The Globular Cluster System of the Edge-On Spiral Galaxy NGC 5170

by

Philippe Fischer

B.Sc., McMaster University, 1987

A THESIS SUBMITTED IN PARTIAL FULFILLMENT
OF THE REQUIREMENTS FOR THE DEGREE OF
MASTER OF SCIENCE
in the Department
of
Physics and Astronomy

We accept this thesis as conforming
to the required standard

[redacted]
Dr. J.E. Hesser

[redacted]
Dr. D.A. VandenBerg

[redacted]
Dr. F.D.A. Hartwick

[redacted]
Dr. P. Driessen

[redacted]
Dr. R. McClure

University of Victoria

June 1989

Supervisor: Dr. J.E. Hesser

ABSTRACT

A CCD study of the edge-on spiral galaxy, NGC 5170, was carried out with the CTIO 4^m telescope to search for its globular cluster system. Three V frames near the galaxy and two removed from it (for background estimation) were analysed. Following median filtering to remove as much of the galaxy light as possible and DAOPHOT analyses, a total of about 130 ± 20 presumed clusters were detected within 2 arcmin of the galaxy's centre above a foreground of Galactic stars and a background of distant galaxies. The photometry does not appear to reach the peak of the globular cluster luminosity function. After incompleteness corrections are made, a total cluster population of $\sim 815 \pm 320$ is inferred. This leads to a specific frequency of $S = 1.3 \pm 0.5$ or $S_{spheroidal} = 3.9 \pm 1.5$, values consistent with what is seen for other isolated disk galaxies. A power law fit to the radial density distribution yields an index of -1.69 ± 0.26, which is again consistent with the globular cluster systems of other galaxies of NGC 5170's total luminosity. The visual distance modulus estimated from the globular cluster luminosity function, 32.3 ± 0.3, agrees well with the Fisher-Tully distance, 32.5, but the agreement may be somewhat fortuitous, inasmuch as the cluster data do not reach the luminosity function peak.

Examiners:

[redacted]

Dr. J.E. Hesser

[redacted]

Dr. D.A. VandenBerg

[redacted]

Dr. F.D.A. Hartwick

[redacted]

Dr. P. Driessen

[redacted]

Dr. R. McClure

Table of Contents

List of Tables

List of Figures

Acknowledgements

I would like to thank Dr. J.E. Hesser for the data, the idea, and his invaluable assistance and Dr. D. VandenBerg for taking care of all the administrative details. I would like to thank Brian Pedersen for always being a year ahead of me, and all the other astronomy graduate students at the University of Victoria. I'd also like to thank the staff of DAO, particularily Peter Stetson (for his great advice and software), Mike Bolte and Michael Pierce. Finally, thanks to Eric Leblanc for his assistance and his sense of humour. Thanks also to NSERC for providing me with a post-graduate scholarship extending over the duration of this project.

Chapter 1

Overview

Globular star clusters have long been recognized in the Milky Way and have been studied extensively by astronomers. They have proven to be very useful tools for the study of stellar evolution; the structure, kinematics, and dynamics of galaxies, and galaxy mergers. More recently, largely as a result of improved detector technology, it has become possible to detect and to study globular clusters in other galaxies, at distances of up to 100 Mpc (1 pc equals 3.09 $\times 10^{13}$ km) (see Hesser 1988 and Harris 1988b for recent reviews)

A globular cluster is a spherical collection of some 100,000 to 1,000,000 stars, contained within a diameter of approximately 60 pc, which form a gravitationally bound system. Globular clusters are believed to contain the oldest stars in the Galaxy (of order 14 billion years old), their formation possibly predating that of the Galaxy itself. As such, these stars generally exhibit very low proportions of elements heavier than helium compared to the sun, presumably because not as much of these elements had yet been created in the interiors of massive stars in this early epoch of galaxy formation. In the Milky Way there have been about 150 globular clusters detected, existing mainly in the halo of the Galaxy, centred on the galactic centre. They exhibit a fall-off in number density from the galactic centre that is proportional to $R^{-2.5}$ (Harris 1986). When one plots the number of clusters versus their intrinsic luminosity (known as the luminosity function, see § 2.IV), the shape of the distribution can be approximated by a gaussian with a mean of $\sim$ –7.2 mag and a dispersion of $\sim$ 1.3 mag (see § 2.VI).

Globular clusters in other galaxies have also been studied out to distances of about 100 Mpc. These studies have concentrated mainly on giant elliptical galaxies, with very little analysis of disk type systems. Therefore, it is not known how significant a role parent galaxy morphology has in determining characteristics of the globular cluster system (GCS).

This thesis presents a study of the GCS of the edge-on spiral galaxy NGC 5170, concentrating on three aspects: 1) the total size of the population; 2) the

radial density distribution; and 3) the distance to the galaxy.

A) Size of the Globular Cluster System

The total sizes of GCSs have been determined for several galaxies (see Harris 1988b for a review). This is of interest as it can reveal much about galaxy formation, and therefore it is important to look for relationships between the size of the GCS and the galaxy luminosity, morphological type, and location. Up to this point, the studies have been primarily of large elliptical galaxies, with some analysis of local group galaxies, and a couple of more distant spirals. For the elliptical galaxies, which are smooth, roughly spherically symmetric, dust-free objects, the globular clusters appear on photographs as swarms of unresolved "stars" near the galaxy. The GCSs of spiral galaxies present a unique observational challenge because of some of the intrinsic properties of these types of galaxies; relatively high dust content, irregular light distribution, smaller total number of globular clusters, and inclination effects. The dust tends to obscure the clusters, while the irregularity of the light renders galaxy light subtraction, and hence cluster photometry difficult. The small number of clusters associated with spirals means that they are hard to detect above a background of Galactic stars, and distant galaxies. As a result, the greatest contrast is obtained by studying spiral galaxies which are seen edge-on. For the galaxies that have been studied, it seems that the most important factor in determining total size of the GCS per unit galaxy luminosity (specific frequency (S), see § 2.VII) is, in fact, environment (Harris 1988a). It has been seen that large galaxies which are located in rich clusters, exhibit values of S about two to three times larger than their relatively isolated counterparts. The exact reasons for this are unknown, and therefore it is essential to accumulate more data for different galaxy types, both isolated, and in rich clusters, in order to obtain a complete data set.

B) Radial Distribution

As has been mentioned above, the Galactic globular clusters exhibit a fall-off from the Galactic centre in radial number density proportional to $R^{-2.5}$. Similar effects have been seen in other galaxies and it has been postulated (Harris 1986),

based on elliptical galaxy data, that the value of the exponent is proportional to the galaxy's intrinsic luminosity. That is, the brighter the galaxy, the less centrally concentrated are its globular clusters. The possible reasons for this vary from different initial formation conditions for large versus small galaxies, resulting in different present day appearances of the GCSs, to identical initial conditions, but different evolutionary effects (i.e., tidal stripping, galaxy mergers, dynamical friction, etc.) for different sized galaxies.

The radial number density distributions for globular clusters are often compared to the parent galaxy halo light distribution. In most elliptical galaxies, both of these fall off in a power law from the galaxy centre. However, it has been shown that in some galaxies, the clusters form a more extended system than the halo light. One possible implication is that the globular clusters formed earlier than the halo stars, when the galaxy was still in the act of collapsing, and was therefore less centrally condensed (Harris 1988a).

C) Distance Determination

Globular clusters have been proposed distance indicators for a considerable period of time. Initially, it was believed that the brightest cluster had a constant luminosity in every galaxy, and, therefore, it was merely necessary to detect this brightest cluster, in order to calculate the distance based on how faint it appeared from earth. This technique is fraught with potential problems. The initial assumption that the intrinsic luminosity of the brightest cluster is constant for all galaxies, is not currently believed to be true. Even if it were, one can never be sure that the brightest cluster has, in fact, been detected, especially when the total number of detected clusters is small. More recently, attempts to use the globular cluster luminosity function (GCLF, see § 2.IV), have proven more satisfactory, but are still not free of serious difficulties. This GCLF can be empirically described as a gaussian, which is believed to have a turn-over luminosity which is remarkably constant over a very large range in parent galaxy luminosity (Harris 1987). The technique involved is to construct the luminosity function for the galaxy in question, fit a gaussian to it, and then see how much of a magnitude shift is required to

superimpose the turn-over on to the the turn-over of the Galactic (or Local Group) GCLF. The size of this shift is equal to the distance modulus of the galaxy.

One problem is that the photometry commonly just attains, or falls just short of, the turn-over luminosity. This means that the gaussian fit will depend largely on the faintest part of the oberved luminosity function, which is the part that has the largest error. This problem may be minor, however, compared to the difficulty associated with the lack of a theoretical understanding and justification for the gaussian form for the GCLF and the magnitude of the luminosity peak. Recent results for several independent distance determinations to the Leo I group of galaxies (see § 2.VI.B) have resulted in the GCLF being the "odd man out", yielding a distance of 6.8 Mpc vs 10 Mpc from the other methods (luminosity fluctuations, planetary nebula, diameter-velocity-dispersion relation, and the Fisher-Tully relationship). Therefore, the universality of the GCLF peak luminosity is seriously brought into question. To solve this problem, it is neccessary to characterize the magnitude of the luminosity peak as a function of galaxy morphology and luminosity observationally, and preferably, theoretically as well. Only in this way, will it be possible to trust GCLF distance determinations, or if the characterization is found impossible, to discard the technique on objective grounds.

Chapter 2

I. Introduction

Globular cluster systems (GCSs) provide a powerful probe of the formation epoch of individual galaxies, and may offer a pure Population II distance indicator (see W.E. Harris 1988b and Hesser 1988 for recent reviews). Beyond a distance (D) of $\sim$ 5 Mpc, globular cluster candidates appear unresolved in $\sim 1''$ seeing, and generally are detected by studies of "star" counts in excess of "background" in the vicinity of galaxies. The available data suggest that: 1) the luminosity functions (LFs) of cluster systems for a wide variety of galaxies can be empirically described by a gaussian. According to W.E. Harris (1987), the peak of this gaussian varies by a very small amount in luminosity over a range of more 1000 in galaxy luminosity. However, more recent distance comparisons suggest that there might be a significant galaxy-to-galaxy variation. 2) The specific frequency (defined by W.E. Harris and van den Bergh (1981) to be the number of globular clusters normalized to a galaxy luminosity of $M_V = -15$, see § VII.A) is a function of the environment in which the galaxy is found. 3) The radial density distribution follows an $R^{\frac{1}{4}}$ law, with larger galaxies appearing to have less centrally concentrated cluster density distributions.

As detailed in the preceding articles, our knowledge is most secure for the large cluster systems of luminous ellipticals, where they are relatively easy to identify and study. Our understanding of the properties of GCSs of spirals is based largely on the Galaxy and M31. In more distant galaxies, the contrast of the cluster systems relative to the foreground stellar component is low. However, to understand which physical elements of the galaxy halo formation process are universal, and which are peculiar to a particular morphological type, we need to

carry out more extensive comparisons between the GCSs of spirals and ellipticals.

To that end, a program to increase the sample of spirals searched for GCSs has been initiated (see H.C. Harris, Bothun, and Hesser 1988). This paper describes the analysis of one spiral galaxy, NGC 5170, from that program. NGC 5170 was chosen for observation because it is seen very near edge-on ($i \approx 90°$), and it has a high luminosity ($M_V = -22.0 \pm 0.25$, see §III.E). Its revised morphological type, 3A (Tully 1988), corresponds to an Sb Hubble classification. The RNGC lists its peculiarities as; an unusually bright centre, equatorial dark lanes and a large degree of diffuseness (Sulentic and Tifft 1973). Investigation of the program frames has further revealed what appears to be a large dust component along the south-west edge, indicating that there is a foreground spiral arm along this edge.

II. Observations

The observations for NGC 5170 ($\alpha_{1950} = 13^h\ 27.12^m$, $\delta_{1950} = -17°\ 42.2'$) were taken on the night of 11/12 February 1986, and the background fields were done the following night. Both nights appeared to be of photometric quality. A total of three galaxy frames and two background frames (one 9′ to the south of the galaxy, and one 9′ to the north) were taken (see Table 1). In addition a total of 34 standard stars (Graham 1982 and Landolt 1983) were measured each night throughout the observing run. All of the frames were taken with the 4^m telescope at the Cerro Tololo Inter-American Observatory (CTIO) using the Johnson V filter and the RCA CCD. This chip has a gain of 10 electrons/ADU and a readout noise of 83 electrons/pixel. There are 300 × 508 pixels, each 0.6 arcsec square yielding an image size of 3 × 5 arcmin (N/S, E/W). Flat-fielding and defringing were done on site using dome flats (median filtered average of 25 done during the afternoon preceding each night) and standard CTIO fringe frames, respectively. Henceforth,

the preprocessed frames are referred to as "original" frames. In the case of multiple exposures, the defringing was applied to the averaged frame. Table 1 summarizes the observations used. The "GAL" and "BKGD" in the "Region" column refer to galaxy frames and background frames, respectively. They are followed by two letters indicating the position with respect to the galaxy centre, or in the cases of "GAL CV" and "GAL CB", the "C" refers to the frame being centred on the galaxy, and the next letter refers to the filter used. The raw and processed (see § III.A) frames are displayed in Fig. 1.

Table 1

Journal of Observations

Region	Exposure (N × sec.)	Airmass (mid–point)	FWHM (arcsec.)
GAL SW	7 × 500	1.29	1.2
GAL NW	7 × 500	1.12	1.2
GAL NE	4 × 900	1.03	0.9
GAL CV	1 × 180	1.02	1.2
GAL CB	1 × 180	1.02	1.2
BKGD SW	4 × 900	1.13	1.2
BKGD NE	4 × 900	1.04	1.2

III. REDUCTION

The reduction procedure for the NGC 5170 frames proceeded in five steps: A) subtraction of the galaxy light and profile-fitting photometry of the remaining objects; B) culling of non-stellar objects; C) calibration of the photometry; D)

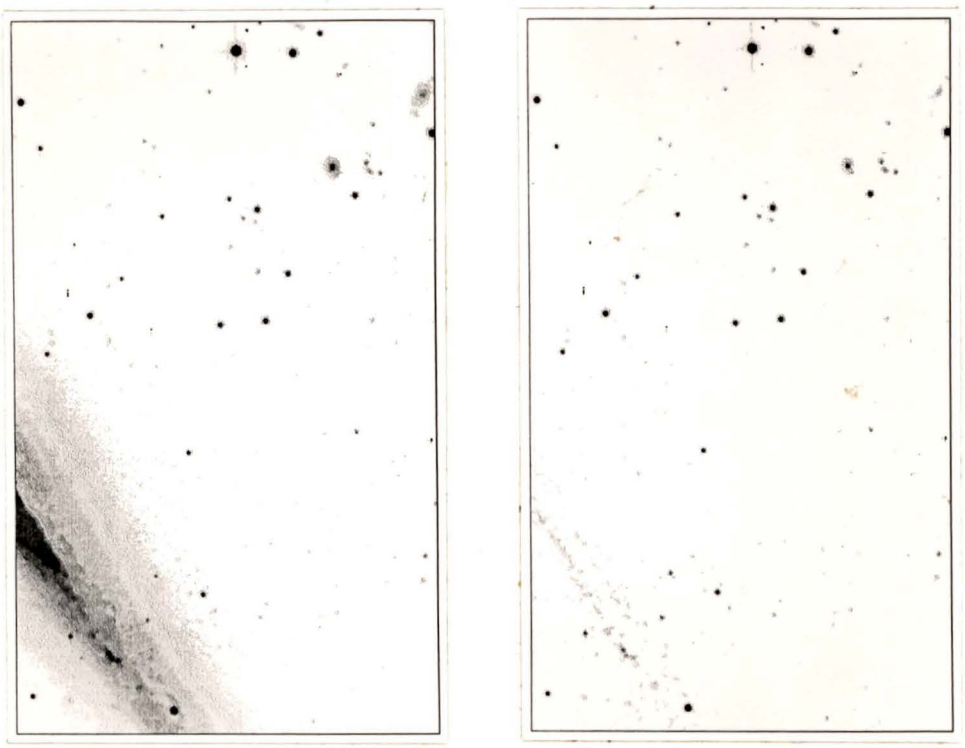

Fig. 1– The three galaxy frames: GAL NE (this page), GAL NW and GAL NE (next page). The raw frame is on the left, while the final galaxy-subtracted frame is on the right . Each frame is $3' \times 5'$, with north on the right, and east on top.

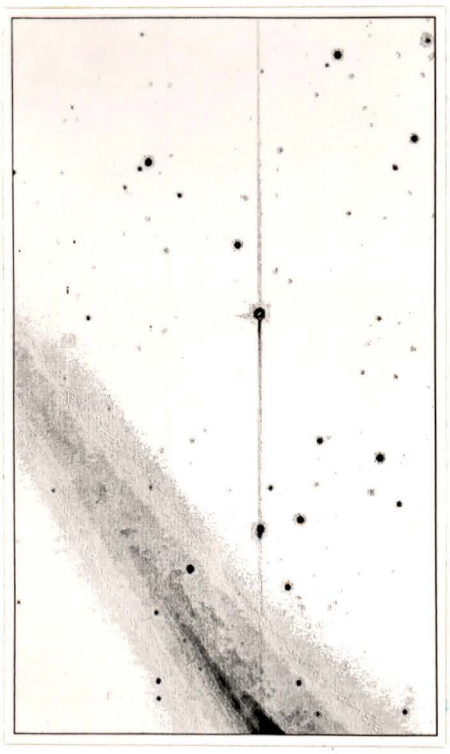

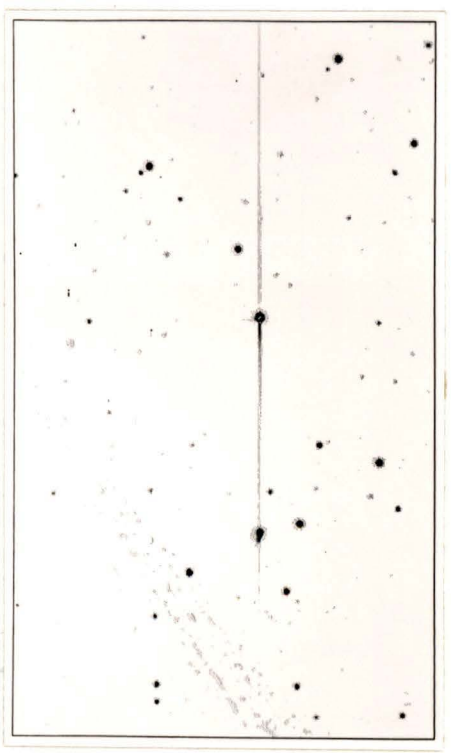

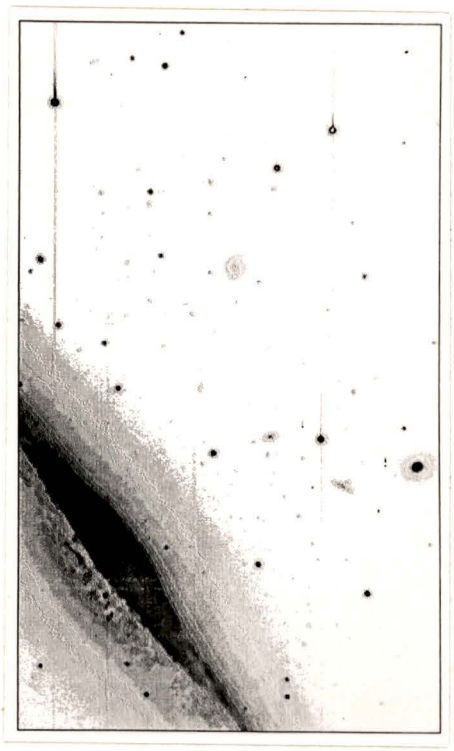

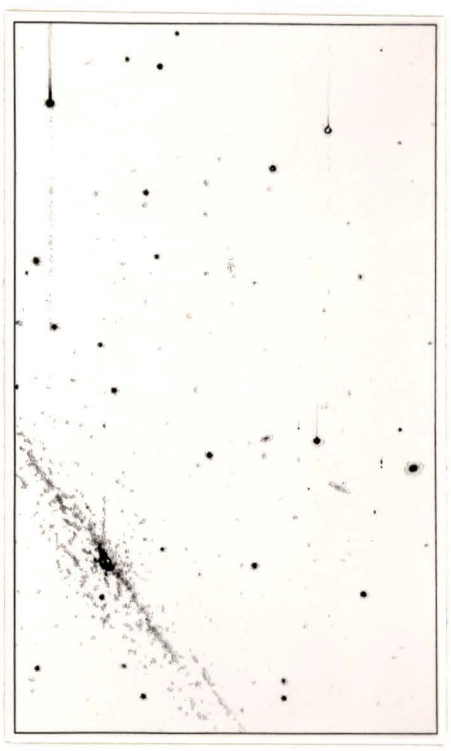

derivation of completeness limits; and E) construction of the luminosity function. Each of these will be described below.

A) Galaxy Subtraction and Cluster Photometry

Since the surface density of globular clusters in known systems approximately follows an $R^{\frac{1}{4}}$ law, where R is the distance from the galaxy centre, it is crucial to be able to detect objects, and perform reliable photometry as close to the centre as possible. This is, however, the region that contains large contributions to the light, and therefore to the photon noise, from the galactic bulge. The introduction of linear CCD detectors has made possible the removal of a substantial component of this diffuse light.

Previous CCD studies of globular cluster systems of nearby galaxies generally focussed on analyses of elliptical parent galaxies, for which galaxy light subtraction is fairly straightforward, and is usually carried out in one of three ways. The first of these is to use an analytical model of the galaxy light (i.e., the de Vaucouleurs (1948) $R^{1/4}$ law) to subtract the galaxy halo (Nelson and Pritchet 1989, private communication). The model provides a smooth approximation to the light, leaving deviations from this smoothness (i.e., globular clusters, foreground stars, and background galaxies) relatively unaffected. Unfortunately, the luminosity profiles of spiral galaxies are much more complex and irregular, owing to such factors as dust, HII regions, inclination effects, etc., which make it difficult to model the light adequately by simple analytical expressions. The second technique involves the fitting of concentric ellipses to the galaxy (Tonry and Schneider 1988), interpolating between the ellipses, and subtracting out the galaxy. This, too, was felt inadequate for NGC 5170, for similar reasons to the first method. The last galaxy subtraction technique involves forming a median filter of the original frame, fol-

lowed by subtraction of the filtered frame from the original (Strom *et. al.* 1981). For an elliptical galaxy, with a smooth light distribution, this can provide very effective galaxy subtraction while leaving stellar-like objects largely unaffected. For a spiral galaxy, a single median filter does not allow one to penetrate adequately into the central region, as too much residual light remains due to steep gradients in the light distribution. Therefore it was deemed necessary to use a series of median filters of different sizes.

The scheme used for NGC 5170 proceeded as follows (see Fig. 2). Initially (Iteration 1) the profile-fitting photometry package DAOPHOT (Stetson 1987) was used on the original frames to find magnitudes for all of the stellar detections. This is a legitimate means of finding NGC 5170 clusters and measuring their luminosities as, due to their large large distance (24 Mpc $\leq$ R $\leq$ 32 Mpc, see § III.E), all clusters will be unresolved and will have star-like point spread functions (PSF). When first applying the FIND routine, it was found that the formula,

$$\sigma = \sqrt{\frac{S + R^2}{N}},$$

(where S, R, and N are, respectively, the sky level, the readout noise in electrons, and the number of frames averaged), for calculating the noise resulted in a detection threshold so low that many spurious detections occurred. The reason is that there is a large contribution to the noise from residual V-band fringing in the thinned RCA CCD. (This problem was doubtless exacerbated by the difficulty of judging, at the telescope, the adequacy of the standard fringe-frame subtraction in the presence of the strong galaxy light.) Consequently the noise was tabulated by direct measurement in several star-free areas on each frame. Using this value for the noise level, the threshold was set at 3.5σ. Aside from this, the procedure followed almost directly that described in the DAOPHOT manual, with FIND

being run twice, the second time after the stars found on the initial pass were subtracted by ALLSTAR, followed by the running of ALLSTAR an additional time. No augmentation to the FIND list with manually detected objects was made.

At this point the star-subtracted frame was median filtered using a filter radius of 12 pixels. The filter used (Stetson 1988, private communication) is a standard circular median filter with one important modification. When the filter approaches within one radius of the edge of the frame, the filter radius is automatically decreased such that there is an equal number of pixels at all radii of the pixel being filtered. This means that in the case of there being a gradient in the light as the edge of the frame is approached, a standard, constant-radius median filter would cause a flattening, or even a reversal of the gradient, while the filter used maintains the low-frequency component with integrity. The price paid is that there is less smoothing effect at the edge of the median filter frames than elsewhere. Next, the filtered frame was subtracted from the original using routines in the Dominion Astrophysical Observatory (DAO) version of VISTA, and a constant was added to the resultant frame to restore the sky level to its original value.

DAOPHOT was then run on the new frame (Iteration 2), and the stars on the new ALLSTAR list were subtracted from the *original* frame. The filtering procedure was repeated with a filter radius of 8 pixels, followed by another run of DAOPHOT (Iteration 3), and a median filter with a radius of 5 pixels, and a fourth application of DAOPHOT (Iteration 4). At each step the new star list was subtracted from the *original* frame and the median filter was run on this *star-subtracted* frame, followed by subtracting this filtered image from the *original* frame. A constant "sky" value is added to the frame following each filtered-frame subtraction to bring the sky level back to its original value.

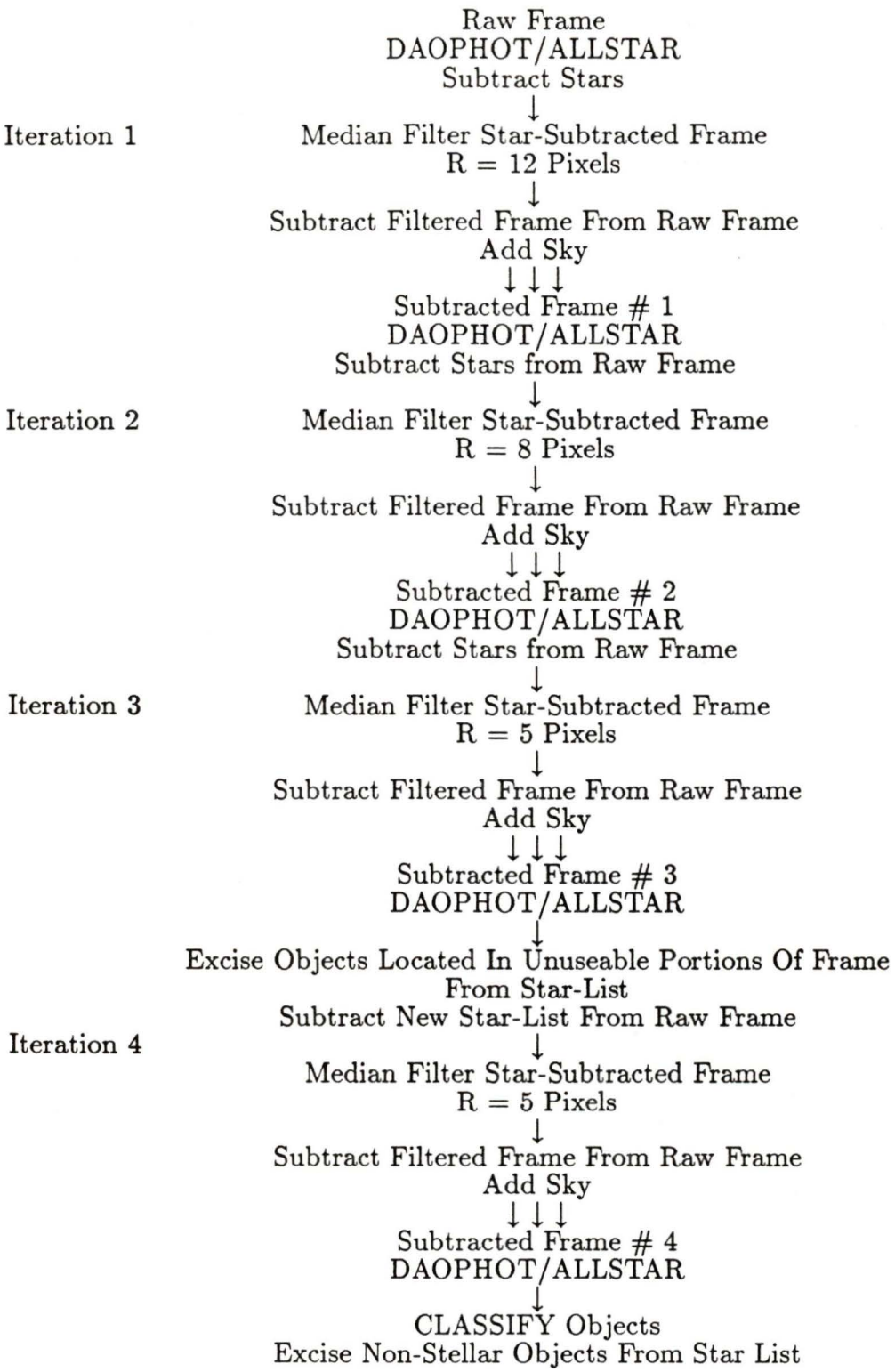

Fig 2– The steps in the galaxy subtraction procedure.

The final median-filtered, galaxy-subtracted frame was then displayed, and every object in the fourth ALLSTAR output list was examined visually on the VICOM display unit at the DAO. Despite this series of median filterings, there was still a substantial residual light contribution near the equator of NGC 5170. In addition, more distant, background galaxies remained on the frame. Furthermore bad columns and charge overflow columns render small portions of each frame unreliable for photometry. Visual inspection was used to decide where the unusable areas of each frame were, and objects detected within these areas were excised from the ALLSTAR list. The total useable area (A_t) of each frame is listed in Table 2, along with the useable area within 2′ of the galactic centre (A_i), and the area beyond this limit (A_o). Once the visual inspection was completed, the modified list of objects was subtracted from the original frame, which was median filtered, using a radius of 5 pixels. A final run of DAOPHOT was carried out, but with the FIND step excluded. The culled AllSTAR list from the previous iteration was used in place of the normal list of *found* objects.

Table 2

Useable Portions of the Frames

Frame	A_i (arcmin^2)	A_o (arcmin^2)	A_t (arcmin^2)
GAL SW	4.02	9.87	13.88
GAL NW	2.28	11.56	13.84
GAL NE	5.89	7.77	13.67
BKGD SW	....	14.95	14.95
BKGD NE	....	15.22	15.22

It is instructive to review the reasoning behind the above photometry procedure. When DAOPHOT is initially run on the original frame, the presence of the galaxy light causes two problems. It results in inaccurate photometry for objects near to and within the galaxy, especially, when (as in our case) objects of interest are inherently faint. It also causes some objects to escape detection altogether. Therefore, a median filter with a big radius (diameter = 24 pixels compared with a typical seeing FWHM = 2 pixels) is initially used. This filter is not so big that it completely smooths out the galaxy light, but it is of sufficient size to totally smooth out any "stellar" objects which escaped detection, and hence subtraction. Therefore, when the filtered frame is subtracted from the original frame, a significant portion of the galaxy light is removed, but undetected objects are left intact. Similarly, the objects with poorly determined magnitudes which ALLSTAR will have either over- or under-subtracted will have the effects of this poor subtraction eliminated in the filtering stage and will similarly be left intact on this first galaxy-subtracted frame. Because this new frame has the galaxy partially removed, the DAOPHOT FIND routine is able to detect more completely objects close to the galaxy and, as well, derive improved photometry for them. This results in a more accurate ALLSTAR subtraction of the objects from the original frame, allowing for the use of a smaller median filter, and a higher degree of galaxy subtraction. This procedure is continued to yet a smaller median filter for even better subtraction of yet higher frequency elements of the diffuse components of the galaxy light.

B) Image Classification

The next stage in the reduction procedure is an attempt to remove non-stellar objects (i.e., galaxies, HII regions, etc.) from the photometry list. As an aid to this goal, the subroutine, CLASSIFY (discussed in W.E. Harris 1988b), was utilized.

This routine calculates intensity moments for all the detected objects allowing for a quantitative means of distinguishing between different types of objects. Primarily the "roundness" moment was used in this application. It is of the form,

$$R = \frac{[(\Sigma x^2 I - \Sigma y^2 I)^2 + (2\Sigma xyI)^2]^{1/2}}{\Sigma I},$$

where x and y are the local coordinate system centred on a particular object in the ALLSTAR list and I is the intensity of a given pixel. When plotted against magnitude, this produces a clearly defined sequence, corresponding to relatively round (stellar) objects, with outliers which are potentially non-stellar. Unfortunately, the roundness moment is sensitive to crowding, and therefore could only be used as a means of flagging potential galaxies, and not as a tool for direct elimination.

Objects with anomalous roundness parameters were then examined by eye, and with the aid of the VISTA CONTOUR command a decision was made whether to keep or discard them. This is the most subjective part of the reduction process, even though an attempt was made to establish a set of objective criteria. Generally, galaxies appear as symmetrical objects on the contour plot, usually with single nuclei, and often with extended structure. In contrast, multiple star detections usually have two (or more) distinct nuclei, although in the case of two stars with very different magnitudes one of the nuclei was often not detectable in this manner. Also, images of blended stars tended to be more asymmetrical than those of galaxies. To counter the possibility of frame-to-frame variations in selection criteria in the difficult borderline objects, all of the frames were examined in as small a time interval as possible, in as consistent a manner as possible. (Appendix A has more details of the classification procedure).

Even though it was impossible to remove all of the galaxies, there are two reasons why attempts are made to remove as many of them as possible. The first

has to do with maximizing the signal (cluster candidates) to noise (foreground stars and background galaxies) in order to reduce the level of uncertainty in the final luminosity function. The second reason is to make the background component of all of the frames (background and galaxy) as homogeneous as possible, thereby facilitating a more accurate and consistent background subtraction. Thus if one or more of the frames has a large background contribution from, say, a cluster of galaxies, then it is hopefully identified in the classification procedure and removed.

C) Calibration

Once the culling procedure was complete, the remaining objects were calibrated to the standard system. Frames of standard stars (Graham 1982 and Landolt 1983) were taken throughout the course of the observing run with both B and V filters. Instrumental magnitudes for the standards were derived using an aperture radius of 25 pixels, while the program objects were measured with a fitting radius of 2 pixels (approximately equal to the FWHM of a stellar image). Therefore it is neccessary to determine zero-point corrections for each frame to put the program objects on the same absolute instrumental scale as the standard stars (so-called "aperture corrections"). This accomplished, one can use transformation equations to obtain Johnson magnitudes for all of the objects. The transformation equations which were used are

$$v = V + A_0 + A_1 \times (B - V) + A_2 \times X + A_3 \times (B - V) \times X \quad \text{and}$$

$$b = B + B_0 + B_1 \times (B - V) + B_2 \times X + B_3 \times (B - V) \times X,$$

where b and v are the instrumental magnitudes, X is the airmass, and B and V are the standard Johnson B and V magnitudes respectively. The standard stars span $10.59 \leq V \leq 16.53$, $-0.23 \leq B\text{–}V \leq 1.32$ and $1.0 \leq X \leq 2.0$. The DAOCCD software package (Stetson 1988, private communication) was used to obtain a

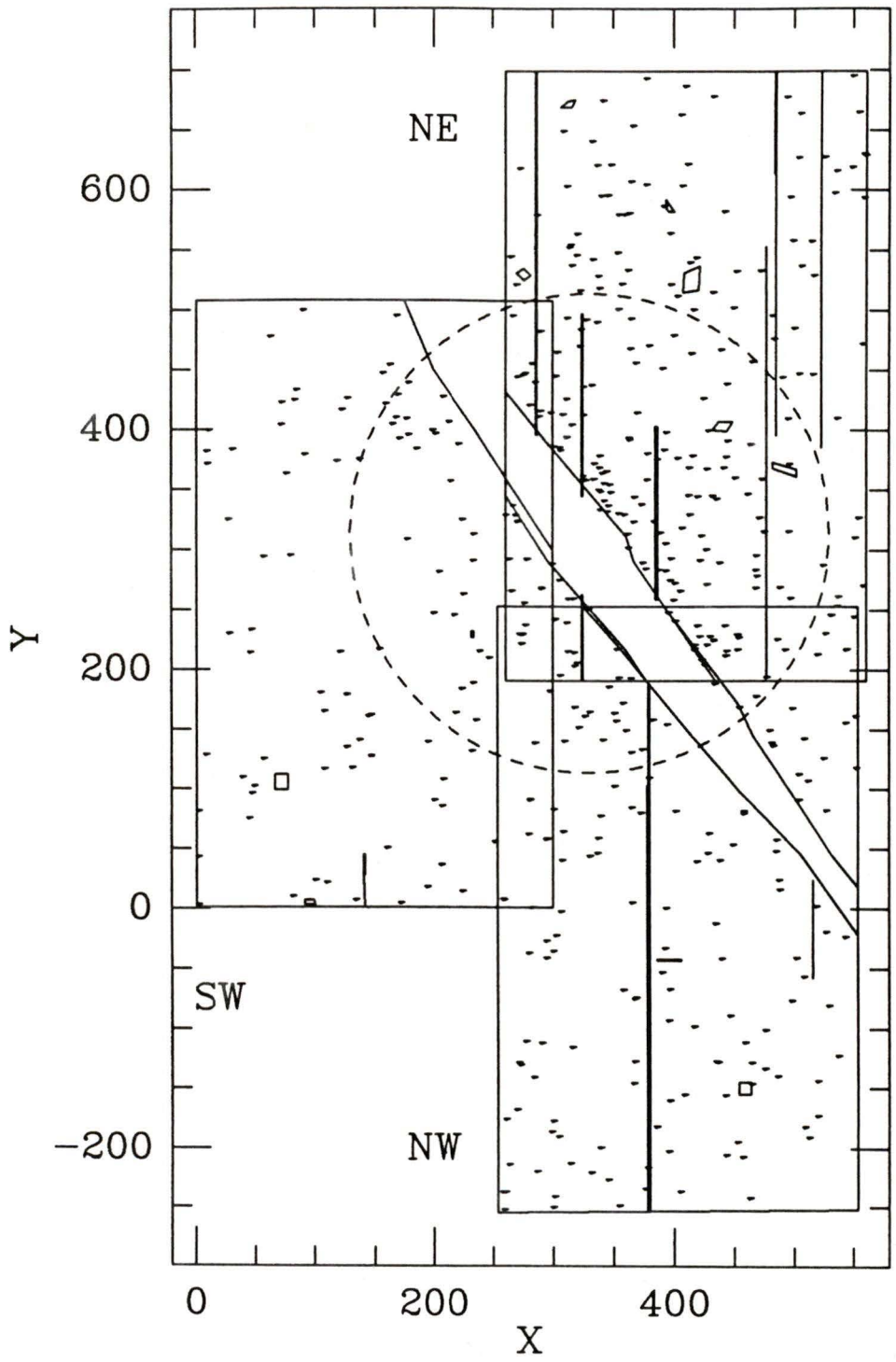

Fig. 3– The three galaxy frames shifted to a common coordinate system. Unuseable portions of the frames are marked, and the points represent the final culled object lists. North is to the right, and east is at the top.

least-squares solution for the the coefficients. For the nights of Feb 11–14, 1986, these values are:

$A_0 = 1.690,$ $B_0 = 1.505,$

$A_1 = 0.020,$ $B_1 = -0.070,$

$A_2 = 0.137,$ $B_2 = 0.260,$

$A_3 = 0.000,$ $B_3 = 0.000.$

The observed scatter in the B and V magnitudes of the standards was 0.015 mag.

Since only V frames were used for the cluster photometry, it is not possible to apply the colour term (A_1). However, assuming that the mean colour for Galactic globular clusters, $\langle B - V \rangle = 0.7$ (Madore 1980), *roughly* holds for NGC 5170, the resulting average change in V is only of order –0.014 magnitudes (i.e., V_{B-V} = V – 0.02(B–V)), and is therefore not a cause for concern.

After calibration, stars which were detected on more than one frame (located on overlapping regions), can be compared for differences in derived magnitudes. Table 3 displays this comparison. Column 2 shows the mean magnitude difference between the frames listed in column 1, while column 3 gives the standard deviation of the distribution. Columns 3 and 4 show the number and magnitude range of these multiply detected stars, respectively. It can be seen from this comparison, that while there are no significant systematic trends (i.e., $|\langle \Delta V \rangle| < \frac{\sigma}{\sqrt{N}}$), there is a fairly large scatter. These regions of overlap are all close to the galaxy, meaning they are in the noisiest portion of the frame, and the stars involved are mostly very faint (median V = 23.34). Therefore this scatter represents an upper limit on the photometry error (see Appendix B for more details on photometry comparisons).

Finally, extinction in the galaxy and internal to NGC 5170 itself must be considered. The Galactic extinction in this direction is A_B = 0.23 mag (Tully 1988). Since $A_V = 3.1 \times (A_B - A_V)$, this implies $A_V \approx 0.17$ mag. This absorption

Table 3

Photometry Comparison

Frames	$\langle \Delta V \rangle$	σ	N	V Range
SW – NW	0.024	0.14	8	17.82–23.76
SW – NE	0.035	0.18	9	20.06–23.75
NW – NE	0.021	0.16	23	19.22–24.29

will not be taken into consideration until the end, and is not included in the photometry tables. As for extinction internal to NGC 5170, all the objects in the final star list are a significant distance from the disk of the galaxy and hence, expected to be in relatively dust-free zones. NGC 5170 is almost certainly not viewed exactly at i = 90°. Inspection of the frame suggests that a spiral arm may be just visible in the south-west and therefore, objects on the south-west side of the galaxy are more likely to be affected by dust. This effect is impossible to quantify, but its affect on the derived luminosity function should be small due to the conservative limit chosen for the unuseable area cut-off.

Tables 8 and 9 show the final, calibrated, culled photometry lists for "stellar" objects in the Inner and Outer regions, respectively, shifted on to the coordinate system of GAL SW (matches Fig. 3). Column 4 shows the distance in pixels from the galaxy centre, while columns 5 and 6 contain the V magnitude, and its ALLSTAR uncertainty. Note however, that since there has been a background subtraction, ALLSTAR will underestimate the amount of noise on the frame, and similarly underestimate the errors, particularly where there has been a large light subtraction. Therefore, the uncertainties shown in Tables 8 and 9 are lower limits to the true uncertainties. Tables 10 and 11 are similar but for the two background frames.

D) Completeness Limits

Now the calibrated objects are binned in terms of luminosity to produce a raw luminosity function. This luminosity function must be corrected for photometric incompleteness (especially at the faint end), and for background contamination (actually foreground stars, and the remaining background galaxies).

The first correction is done using a laborious but straightforward procedure, artificial star simulations. Stars of known magnitude are generated from the empirical PSF for addition to the frame using ADDSTAR according to a luminosity function generated by the IASG (Institute of Advanced Studies Galaxy) model (Ratnatunga, Bahcall, and Casertano 1989). In a typical application of this procedure to crowded field photometry of Galactic globular clusters, the added stars generally total about 10% of the original star list (c.f., Stetson and Harris 1988). However, our frames were so uncrowded (GAL NE, the most crowded frame contains only 257 culled objects), and the majority of the detections faint enough, that it was felt that 200 hundred stars could be added per simulation without affecting the crowding character of the frame. The new frame was subjected to an identical reduction procedure as the original frame, and the number of recovered objects was tabulated. The fraction of recovered objects over added objects (f) is a function of input magnitude: it is equal to 1.0 at the bright end, remains relatively constant over a large range in luminosities, and then falls off very rapidly as the frame limit is approached. This ratio is used to correct each bin. Tables 4, 5, 6, and 7 display the results of the artificial star simulations for each frame for the Inner region (within 2′ of the galaxy's centre) and the Outer region. Columns 2 and 6 are the number of objects which were originally observed on the frame. Columns 3 and 7 are the number of added stars, and columns 4 and 8 are the

number of recovered stars. For each frame, the faintest bin retained for luminosity function construction is the one with a completeness level $\geq 59\%$. These are displayed between the horizontal lines in the four tables. Since the bins have a width of 0.5 magnitudes, the true cut-off magnitudes are really 0.25 magnitudes fainter than the cut-off bins.

Fig. 4 shows plots of ΔV (true minus observed V mag) vs V for the three galaxy frames combined, separated into the Inner and Outer regions. Only objects up to the completeness limits for each field are plotted. A bin-by-bin analysis of ΔV has been made (see Appendix C) for all five frames. Means and standard deviations were calculated for each bin, and slopes ($\frac{\Delta V}{V}$) were calculated for the Inner and Outer regions of each frame, in order to search for systematic errors in the star recovery process. In all eight cases there was a negligible systematic effect (the largest slope occurred for the Outer region of GAL NE, 11.0 $\times 10^{-4}$).

E) Galaxy Photometry and Other Parameters

Photometry was performed on NGC 5170 using both B and V frames centred on the galaxy (GAL CV and GAL CB). The main purpose was to derive an accurate B–V colour index for the galaxy, which could be used in conjunction with the Fisher-Tully relation in B to estimate M_V. This photometry proceeded in four steps: 1) subtraction of bright stars; 2) removal of contamination from bright columns and cosmetic faults on the CCD; 3) totalling of the flux; and 4) calibration of the magnitudes.

Star-subtraction was accomplished using DAOPHOT and ALLSTAR. Galaxies and bad pixels were removed by median filtering the contaminated areas. The flux was tabulated as as a simple addition over the whole frame in the following

Table 4

Artificial Star Simulations GAL SW

	Inner				Outer			
Bin	N_{obs}	N_{add}	N_{rec}	f_i	N_{obs}	N_{add}	N_{rec}	f_o
19.25	0	21	21	1.00	3	43	42	0.98
19.75	1	18	18	1.00	3	49	47	0.96
20.25	3	19	19	1.00	3	62	61	0.98
20.75	0	26	25	0.96	1	78	76	0.97
21.25	2	35	35	1.00	4	107	105	0.98
21.75	0	40	39	0.98	6	82	79	0.96
22.25	1	47	46	0.98	7	118	114	0.97
22.75	3	41	41	1.00	8	100	92	0.92
23.25	9	54	52	0.96	13	118	112	0.95
23.75	20	53	45	0.85	13	117	80	0.68
24.25	0	69	15	0.22	5	144	39	0.27
24.75	1	17	0	0.00	1	47	3	0.06
Totals	40	440	356		67	1065	850	

manner,

$$Flux = \Sigma(I_i - sky)$$

where I_i is the pixel intensity and sky is the value obtained from the DAOPHOT sky command. DAOPHOT uses a very robust estimator for this sky value, which will yield accurate values even in the presence of the strong galaxy light. This is borne out by the excellent agreement between the value returned by sky and direct measurement of areas on the frame furthest from galaxy contamination.

Table 5

Artificial Star Simulations GAL NW

	Inner				Outer			
Bin	N_{obs}	N_{add}	N_{rec}	f_i	N_{obs}	N_{add}	N_{rec}	f_o
18.25	1	5	5	1.00	1	36	36	1.00
18.75	0	8	8	1.00	1	34	34	1.00
19.25	2	8	8	1.00	0	56	56	1.00
19.75	1	14	13	0.93	1	46	46	1.00
20.25	2	12	12	1.00	4	64	64	1.00
20.75	0	18	15	0.83	2	69	67	0.97
21.25	0	20	20	1.00	7	105	103	0.98
21.75	0	24	23	0.96	7	96	93	0.97
22.25	3	21	20	0.95	11	116	113	0.97
22.75	2	38	38	1.00	9	120	118	0.98
23.25	8	30	29	0.97	20	134	129	0.96
23.75	15	40	37	0.93	21	133	126	0.95
24.25	8	21	13	0.62	31	155	117	0.75
24.75	2	33	4	0.12	4	180	35	0.19
25.25	1	12	2	0.17	2	42	2	0.05
Totals	45	304	247		121	1386	1139	

The standard deviation of the flux is given by,

$$\sigma = \sqrt{\Sigma(I_i + sky + R^2)},$$

where R is the readout noise in electrons. Calibration was accomplished by first correcting the instrumental magnitudes for absorption, both internal ($A_B = 0.67$

Table 6

Artificial Star Simulations GAL NE

	Inner				Outer			
Bin	N_{obs}	N_{add}	N_{rec}	f_i	N_{obs}	N_{add}	N_{rec}	f_o
19.250	3	15	14	0.93	1	33	33	1.00
19.750	2	35	34	0.97	0	38	38	1.00
20.250	2	39	39	1.00	3	51	50	0.98
20.750	0	42	42	1.00	1	56	55	0.98
21.250	0	48	46	0.96	1	54	52	0.96
21.750	0	58	57	0.98	3	64	62	0.97
22.250	3	48	48	1.00	6	66	63	0.95
22.750	11	74	72	0.97	5	79	78	0.99
23.250	23	68	68	1.00	4	95	92	0.97
23.750	39	71	69	0.97	9	92	91	0.99
24.250	43	71	67	0.94	22	127	115	0.91
24.750	37	74	44	0.59	28	103	66	0.64
25.250	3	104	23	0.22	7	111	12	0.11
Totals	166	747	623		90	969	807	

(Tully 1988)) and Galactic (A_B = 0.23 (Tully 1988)), for a total of 0.90 in B and 0.68 in V. These new instrumental magnitudes were then increased by 25, to give them a zero-point consistent with the ALLSTAR photometry. It was then possible to calibrate the magnitudes using the relationship given in § III.C. The values thus derived are V_{cor} = 10.9 ± 0.004, and B_{cor} = 11.5 ± 0.01. These are not true apparent magnitudes as the CCD was not large enough to image

Table 7

Artificial Star Simulations BKGD SW and BKGD NE

	BKGD SW				BKGD NE			
Bin	N_{obs}	N_{add}	N_{rec}	f_o	N_{obs}	N_{add}	N_{rec}	f_o
18.75	2	27	27	1.00	1	16	16	1.00
19.25	0	38	38	1.00	1	31	31	1.00
19.75	3	40	39	0.98	0	42	42	1.00
20.25	2	42	42	1.00	0	41	40	0.98
20.75	1	50	50	1.00	4	51	51	1.00
21.25	3	56	52	0.93	5	40	38	0.95
21.75	4	78	77	0.99	6	61	55	0.90
22.25	10	83	81	0.98	4	65	65	1.00
22.75	12	63	62	0.98	5	76	74	0.97
23.25	20	97	94	0.97	11	74	71	0.96
23.75	31	101	99	0.98	18	91	90	0.99
24.25	49	109	105	0.96	33	83	77	0.93
24.75	59	114	71	0.62	59	110	84	0.76
25.25	15	110	17	0.15	11	109	30	0.28
25.75	3	132	7	0.05	3	109	6	0.06
Totals	214	1140	861		161	999	770	

the whole galaxy. In fact, despite the fortuitous galaxy alignment (the galaxy runs from corner to corner on the CCD), the diameter imaged (5.8 arcminutes), is slightly short of the diameter of the 25 mag/arcmin^2 surface brightness level (6.1 arcminutes (Tully 1988)), which is believed to contain approximately 80% of

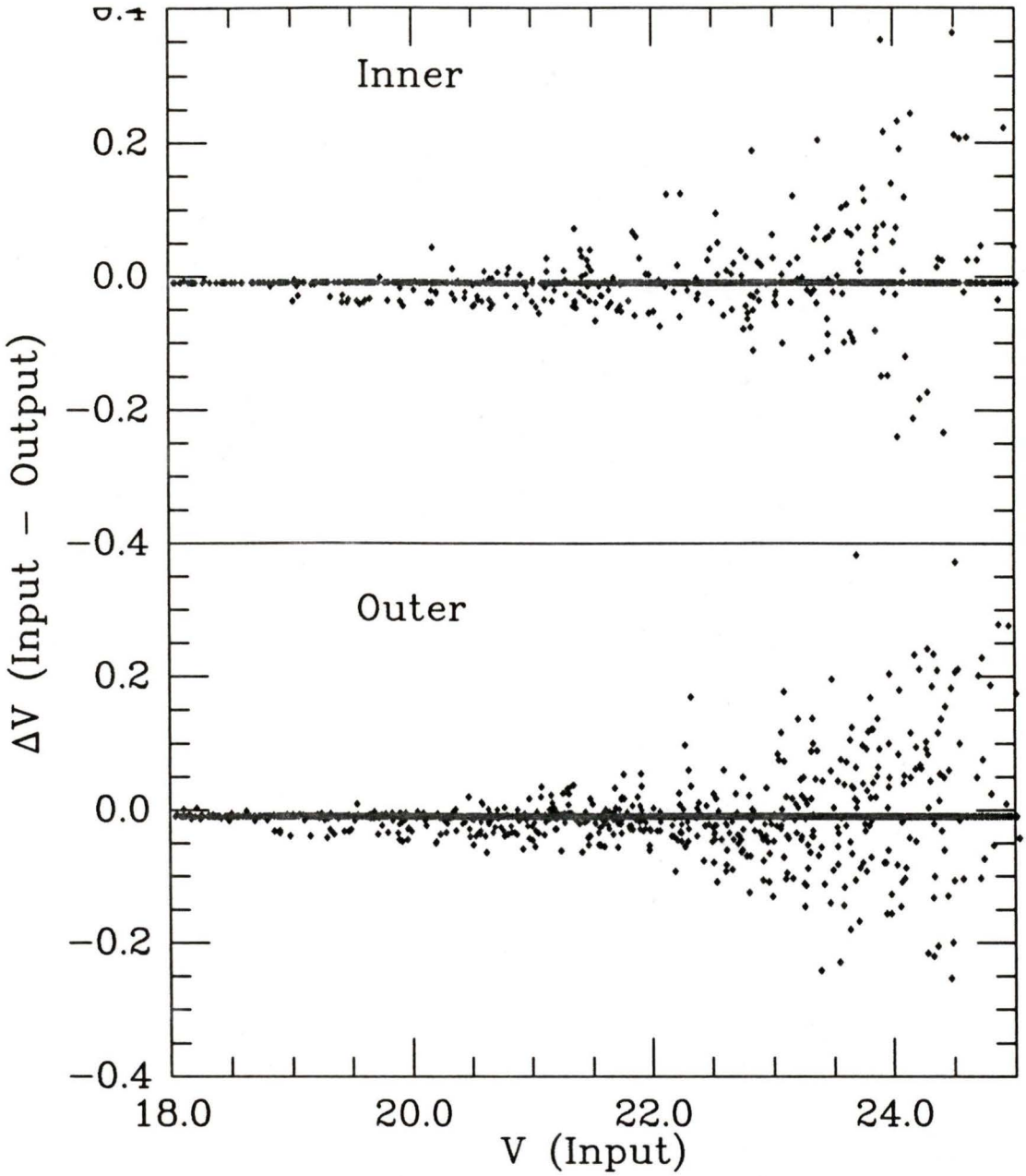

Fig. 4– Differences in magnitude for the artificial star simulations on the three galaxy frames combined. "Inner" is for stars within 2 arcminutes of the galactic centre (total of 1229 stars), and "Outer" are all the rest (total 2784 stars).

the galaxy light (Pierce 1989, private communication). Therefore we are probably missing around 30% of the light. This however is almost certainly a second-order effect in the B–V colour index, 0.62 ± 0.01, which is our primary interest, and which is in excellent agreement with Table 4B of de Vaucouleurs (1977) for a type 3 galaxy [$\langle (B-V)^{\circ}_{T} \rangle = 0.64 \pm 0.08$]. The errors quoted here derive solely from the above formula for σ.

NGC 5170 has a corrected B magnitude of $B_{cor} = 10.9$ (Tully 1988). As well, the same catalogue lists an H magnitude of 8.30 for this galaxy. The raw 21 cm line profile has a width of W = 629 km s^{-1} which is corrected for turbulence to $W_{cor} = 591$ s^{-1}. Using the Fisher-Tully relationship it is possible to derive intrinsic magnitudes for the galaxy (M_H and M_B) and therefore to obtain a distance modulus. The Fisher-Tully relationship is given by,

$$M_B = B_1 \times Log(W_{cor}) + B_2, \quad \text{and}$$

$$M_H = H_1 \times Log(W_{cor}) + H_2,$$

where $B_1 = -7.3$, $B_2 = -1.18 \pm 0.25$, $H_1 = -9.25$, and $H_2 = 1.40 \pm 0.14$ (Pierce and Tully 1988). These yield $M_B = -21.41 \pm 0.25$ ($M_V = -22.0 \pm 0.25$), and $M_H = -24.24 \pm 0.14$, which in turn lead to distance moduli of $(m\text{-}M)_B = 32.3 \pm 0.25$ and $(m\text{-}M)_H = 32.5 \pm 0.14$, respectively. $(m\text{-}M)_o = 32.5 \pm 0.14$, corresponding to a distance of 31.6 Mpc, is adopted as the Fisher-Tully luminosity distance for future discussion. [The H-band value is preferred due to the unreliable nature of B_{cor} which was derived from Harvard magnitudes (de Vaucouleurs, de Vaucouleurs, and Corwin 1976) using standard transformation formulae (Tully 1988).]

Radial velocity data for NGC 5170 range from 1347 km s^{-1} (Tully 1988) to 1432 ± 20 km s^{-1} (optical absorption spectra, Sandage 1978) to 1435 km s^{-1} (Eastmond and Abell 1978). These have all been corrected for a motion of 300 km s^{-1} towards l = 90°, b = 0°. Despite the apparent consistency between the

latter two values, the former one is adopted for the purposes of the paper. The reasons are that: Sandage cites his plate quality as poor, and Eastmond (1977) quote an r.m.s. error of 100 km s^{-1}. Tully, however, uses HI observations, and quotes an r.m.s. error of 10 km s^{-1}. Using 1347 km s^{-1} and a Hubble constant, H_o = 75 km s^{-1} Mpc^{-1}, Tully derives a distance of 24 Mpc to NGC 5170. This is obtained by using a model that describes velocity perturbations in the vicinity of Virgo (Tully and Shaya 1984), which are significant for the galaxy in question owing to its location nearby and behind the Virgo cluster. This position causes a large retardation in NGC 5170's recession velocity. The value of 24 Mpc is adopted as the radial velocity distance to NGC 5170 for all subsequent discussion. However, because of the disparity in the Fisher-Tully luminosity and the radial velocity distances, both will be used in future discussions.

Table 8
Inner Region Photometry

Star	X	Y	R	V	σ
135	364.59	130.77	186.52	23.96	0.10
137	373.29	133.37	185.81	23.80	0.07
140	284.64	138.85	180.82	23.79	0.08
143	308.81	140.68	174.55	23.92	0.10
145	340.89	141.69	172.66	24.08	0.13
148	359.92	149.54	167.21	18.49	0.03
149	321.00	151.82	162.39	24.46	0.21
150	394.24	154.48	172.09	22.27	0.04
152	351.93	157.41	158.15	22.28	0.04
153	235.28	157.87	182.41	23.34	0.09
154	382.57	158.59	164.16	23.24	0.07
156	325.84	161.59	152.44	23.28	0.07
159	218.36	164.13	186.64	23.72	0.14
160	350.54	164.20	151.23	23.52	0.11
162	330.23	165.02	148.96	23.44	0.13
164	453.86	168.84	191.05	20.42	0.02
165	317.35	168.98	145.52	23.97	0.10
166	357.59	172.72	144.00	23.14	0.05
167	468.24	177.81	194.31	22.88	0.06
170	296.76	182.57	135.46	23.22	0.32
171	223.71	183.89	167.76	20.49	0.03
172	433.40	188.47	162.85	22.62	0.06
173	232.99	188.90	158.06	22.65	0.07
174	363.81	193.15	125.57	23.35	0.05
175	354.20	193.35	123.11	24.26	0.15
176	476.64	194.04	189.73	24.88	0.20
177	305.27	195.29	121.16	24.60	0.16
178	317.45	203.37	111.28	24.52	0.11
179	425.03	204.58	145.15	23.76	0.10
180	319.69	205.85	108.59	23.55	0.06
181	422.92	208.26	141.00	22.12	0.04
182	246.30	210.14	133.14	18.67	0.01
183	443.02	212.10	152.44	24.08	0.10
187	316.76	214.30	100.51	24.46	0.08
188	312.09	215.30	100.23	23.62	0.07
189	238.74	215.61	133.93	23.65	0.08
190	443.70	216.13	150.29	24.83	0.19
191	452.69	216.85	156.77	19.17	0.06
193	491.82	217.19	188.88	24.61	0.21
195	352.45	217.63	99.02	19.25	0.05

Table 8(cont.)

Star	X	Y	R	V	σ
196	416.76	217.87	129.73	24.36	0.17
197	416.86	220.98	127.51	24.57	0.14
198	427.00	221.14	134.54	24.59	0.21
199	273.79	221.98	107.62	23.09	0.12
200	432.37	224.80	136.05	24.20	0.23
201	485.56	225.65	179.21	23.93	0.10
202	453.62	227.17	151.36	23.51	0.14
203	429.46	227.84	131.86	23.86	0.25
204	421.00	228.02	125.45	24.45	0.17
205	452.36	229.31	149.10	19.83	0.04
206	274.30	229.67	100.84	23.38	0.11
208	271.90	230.05	101.87	23.17	0.09
210	344.68	231.73	83.62	24.21	0.12
212	441.99	236.98	136.21	24.14	0.11
213	419.31	237.06	118.15	23.93	0.11
214	277.19	237.66	92.60	19.92	0.03
215	310.95	239.52	76.77	24.86	0.12
216	400.80	240.98	101.95	23.55	0.13
217	301.43	242.39	76.94	24.17	0.14
219	217.24	245.38	131.67	23.58	0.15
221	199.61	246.96	146.28	23.43	0.11
222	395.57	248.14	93.18	23.85	0.13
223	329.23	250.83	63.15	24.02	0.12
225	275.97	256.19	78.86	24.30	0.12
226	399.63	258.33	89.43	24.26	0.09
227	316.66	259.51	55.99	22.31	0.05
228	312.40	259.74	56.91	24.61	0.20
229	496.65	259.82	175.58	23.86	0.10
231	224.89	263.02	116.48	23.72	0.09
232	405.03	266.09	89.32	24.00	0.08
233	265.47	266.17	80.01	23.97	0.14
234	290.03	268.25	60.49	23.41	0.05
235	467.71	268.45	145.39	23.03	0.09
236	487.36	269.08	164.00	23.93	0.10
238	426.97	271.58	106.17	23.99	0.09
239	400.40	272.55	82.01	23.46	0.05
240	304.86	274.91	46.26	23.24	0.09
241	396.44	275.09	77.30	24.22	0.08
242	468.33	278.31	143.21	24.59	0.16
243	204.07	281.56	129.68	23.55	0.09

Table 8(cont.)

Star	X	Y	R	V	σ
244	392.90	283.04	70.43	24.46	0.12
245	467.36	283.35	141.09	24.44	0.12
246	386.94	283.46	64.93	24.18	0.17
247	376.70	284.29	55.65	23.66	0.08
248	524.17	287.45	196.34	24.52	0.19
249	298.75	288.50	40.04	23.32	0.07
250	437.72	289.65	110.79	24.25	0.13
251	374.18	289.72	50.73	24.52	0.09
252	233.20	290.83	99.17	23.98	0.20
253	421.70	291.66	94.74	24.00	0.13
254	278.25	292.25	55.79	23.18	0.06
255	263.38	292.61	69.61	23.90	0.11
256	397.50	292.98	71.04	24.52	0.12
259	467.96	295.57	139.55	24.31	0.17
260	426.44	300.28	97.77	24.81	0.14
261	361.92	302.02	34.43	24.56	0.21
262	392.83	305.43	63.78	22.51	0.05
263	177.03	308.37	152.70	20.17	0.02
265	422.37	312.01	92.76	22.93	0.07
266	233.38	313.05	96.25	23.62	0.17
267	361.50	313.74	31.87	24.75	0.18
268	388.30	314.39	58.67	24.00	0.09
269	494.82	315.39	165.20	23.23	0.04
270	474.41	315.51	144.79	23.72	0.05
271	406.38	318.64	76.89	23.83	0.05
272	366.39	323.40	37.95	20.48	0.03
273	270.64	323.80	59.80	23.83	0.08
274	383.29	323.98	54.58	22.99	0.05
275	223.90	324.80	106.28	22.23	0.06
278	470.38	326.91	141.34	22.82	0.04
279	260.73	328.88	70.49	23.51	0.09
280	268.28	329.20	63.21	24.43	0.13
281	358.56	329.48	32.82	23.76	0.09
282	412.76	329.62	84.59	24.42	0.08
283	353.81	330.39	29.22	22.78	0.07
284	344.62	331.79	23.28	23.60	0.17
285	338.89	333.60	21.70	23.72	0.08
286	345.32	337.03	27.88	24.10	0.10
287	266.44	337.17	67.31	24.56	0.12
288	373.19	338.04	49.76	24.82	0.18

Table 8(cont.)

Star	X	Y	R	V	σ
289	342.01	340.77	29.51	24.16	0.13
290	435.18	342.64	109.37	24.32	0.07
291	366.83	344.15	47.90	23.93	0.20
292	419.38	344.71	94.87	23.97	0.06
293	431.45	344.80	106.38	24.11	0.16
294	412.20	345.34	88.32	24.54	0.11
295	460.75	346.57	135.11	22.71	0.05
296	347.26	347.95	38.27	23.44	0.13
297	339.22	348.71	36.03	24.79	0.22
298	337.26	350.18	37.00	23.65	0.09
299	346.39	354.44	43.79	24.39	0.14
300	341.80	355.59	43.35	24.48	0.23
301	214.08	356.92	123.27	23.71	0.13
302	326.86	358.03	44.14	24.22	0.16
303	377.28	358.66	65.32	24.41	0.13
304	333.74	358.89	45.10	24.40	0.12
305	473.10	358.92	150.34	24.98	0.24
306	324.40	358.97	45.29	23.34	0.11
307	450.38	359.98	129.22	23.75	0.09
308	324.63	361.44	47.72	24.36	0.19
309	340.38	363.92	51.08	24.53	0.17
310	343.96	365.46	53.44	23.39	0.07
311	427.08	367.39	111.13	24.89	0.15
312	440.98	368.63	124.04	24.70	0.17
313	338.03	368.67	55.33	23.83	0.09
314	412.67	368.72	99.46	24.39	0.11
315	495.73	371.25	175.70	23.15	0.12
317	333.99	372.11	58.29	22.87	0.05
320	386.08	375.51	83.50	24.01	0.17
321	402.80	376.38	96.16	24.42	0.11
322	443.13	377.50	130.07	24.20	0.16
323	338.65	378.53	65.18	23.31	0.05
324	415.64	378.69	107.63	23.85	0.11
326	378.13	380.39	82.23	24.34	0.16
328	306.00	383.14	73.09	23.96	0.09
330	391.79	383.72	93.42	22.72	0.06
331	184.85	384.24	160.93	22.83	0.09
332	304.88	385.35	75.54	23.28	0.06
333	300.54	386.24	77.90	24.23	0.13
334	463.56	387.87	152.96	23.28	0.09

Table 8(cont.)

Star	X	Y	R	V	σ
335	220.99	388.15	131.54	23.78	0.15
336	444.43	391.07	138.28	24.82	0.10
337	362.86	391.81	84.63	24.46	0.16
338	170.72	392.32	177.17	23.83	0.20
339	362.73	393.74	86.36	24.83	0.22
340	310.78	393.99	82.20	24.88	0.12
341	177.90	395.70	172.34	23.85	0.17
342	201.15	396.31	152.60	21.12	0.03
343	393.33	397.93	105.38	24.68	0.28
344	198.56	399.52	156.51	23.51	0.10
345	428.33	399.67	130.71	22.75	0.05
348	315.40	404.43	91.56	23.66	0.07
349	164.46	404.59	188.39	23.49	0.09
350	212.31	406.68	149.52	23.58	0.12
351	176.59	409.07	180.18	22.89	0.09
352	494.74	409.52	190.76	23.74	0.09
353	167.48	409.96	188.43	19.75	0.01
355	288.67	411.34	105.63	24.27	0.10
356	324.90	412.42	98.55	22.48	0.07
357	307.95	412.92	101.29	23.26	0.10
358	369.67	414.29	108.01	23.98	0.10
359	297.95	414.54	105.43	22.92	0.07
360	289.68	416.06	109.62	23.57	0.09
362	280.74	421.07	117.72	23.62	0.11
367	311.08	426.14	113.68	23.73	0.19
368	424.71	426.70	147.47	24.66	0.16
369	207.34	427.70	166.99	21.29	0.03
370	169.13	429.14	197.54	23.73	0.10
372	325.04	435.82	121.93	24.02	0.07
373	331.97	437.74	123.78	18.92	0.04
374	443.90	438.55	169.04	24.50	0.13
375	178.24	438.85	196.24	23.65	0.15
376	284.78	439.77	133.55	23.40	0.12
378	270.37	444.66	143.49	24.60	0.10
379	302.17	445.18	134.04	22.67	0.07
380	275.39	446.16	142.88	23.75	0.07
384	276.94	447.69	143.72	24.74	0.15
385	390.55	451.39	150.31	24.41	0.09
387	282.50	455.48	149.14	24.80	0.23
388	368.63	456.23	147.50	24.73	0.16

Table 8(cont.)

Star	X	Y	R	V	σ
389	464.77	456.87	196.67	23.89	0.09
390	414.32	464.18	172.43	24.56	0.16
391	303.74	465.01	153.23	23.43	0.12
392	439.12	467.22	188.34	23.29	0.07
393	363.82	468.07	157.84	23.49	0.11
394	322.07	470.19	156.39	20.16	0.03
395	379.52	470.66	164.43	24.38	0.13
399	400.06	478.97	179.39	23.90	0.11
400	289.27	482.63	173.41	19.24	0.02
401	322.98	483.76	169.91	24.75	0.17
403	336.55	490.03	176.19	23.75	0.14
404	327.28	492.03	178.07	24.60	0.11
405	364.34	493.20	182.55	24.60	0.17
406	311.43	493.48	180.42	24.46	0.17
408	266.56	495.41	192.08	24.14	0.11
412	353.86	500.81	188.39	23.37	0.13

Table 9
Outer Region Photometry

Star	X	Y	R	V	σ
1	258.92	−252.34	570.72	22.86	0.06
2	299.72	−250.30	565.07	23.48	0.10
3	353.87	−248.77	563.27	23.35	0.09
4	462.49	−242.28	571.91	21.41	0.02
5	300.35	−241.55	556.30	23.65	0.14
6	258.06	−237.63	556.23	22.14	0.22
7	259.76	−237.39	555.78	20.78	0.11
8	404.73	−237.20	556.27	24.20	0.16
9	375.60	−234.28	550.18	24.42	0.19
10	345.15	−226.61	540.81	23.95	0.13
11	330.94	−220.32	534.30	21.23	0.02
12	285.84	−219.50	535.27	24.22	0.15
13	377.30	−215.99	532.11	21.53	0.03
14	263.08	−213.41	531.57	23.11	0.08
15	313.40	−212.49	526.72	23.08	0.14
16	456.27	−206.87	536.02	22.84	0.06
17	442.61	−205.73	531.85	23.40	0.11
18	338.43	−199.26	513.32	22.27	0.02
19	452.02	−194.45	522.95	23.66	0.10
20	512.09	−190.50	536.46	21.37	0.02
21	304.06	−189.90	504.53	23.18	0.10
22	298.20	−185.85	500.82	24.02	0.14
23	508.45	−182.04	527.27	22.69	0.04
24	385.20	−181.97	499.05	23.83	0.12
25	299.70	−177.43	492.32	22.98	0.05
26	260.44	−176.22	495.06	24.42	0.14
27	519.69	−173.04	522.79	24.16	0.15
28	269.31	−168.14	485.88	18.44	0.01
29	395.89	−160.57	479.15	24.19	0.10
30	442.01	−156.06	483.29	22.73	0.05
31	408.00	−155.49	475.97	24.37	0.12
32	464.21	−146.73	479.96	19.91	0.01
33	366.10	−146.12	461.54	23.77	0.12
34	519.68	−143.77	495.64	22.41	0.05
35	283.28	−141.21	457.54	24.41	0.12
36	485.49	−139.76	479.76	24.44	0.19
37	475.02	−133.57	470.57	20.94	0.02
38	272.30	−130.59	448.25	23.67	0.10
39	271.14	−128.70	446.53	24.13	0.15
40	464.05	−128.61	462.55	23.81	0.08

Table 9(cont.)

Star	X	Y	R	V	σ
41	436.13	−128.10	454.73	20.43	0.03
42	434.29	−127.60	453.81	24.11	0.23
43	366.92	−127.59	443.14	23.42	0.10
44	536.80	−122.56	483.20	22.32	0.04
45	315.55	−115.46	429.67	21.80	0.02
46	289.94	−111.93	427.76	23.39	0.14
47	458.32	−111.34	444.36	22.20	0.05
48	276.92	−110.55	427.79	24.44	0.14
49	475.49	−100.85	439.73	22.75	0.04
50	415.96	−98.23	421.15	23.77	0.10
51	394.91	−92.95	412.13	17.77	0.03
52	445.95	−88.77	419.21	21.54	0.12
53	528.93	−80.58	442.04	24.06	0.14
54	497.33	−76.65	425.11	22.47	0.04
55	366.90	−75.03	390.79	22.78	0.23
56	367.96	−74.23	390.10	22.97	0.27
57	357.33	−67.28	382.26	22.20	0.04
58	396.23	−67.18	386.93	23.16	0.07
59	508.22	−56.69	411.45	23.88	0.15
60	389.59	−53.20	372.04	24.05	0.18
61	438.90	−41.70	372.09	23.58	0.06
62	501.48	−40.81	394.22	20.13	0.01
63	294.20	−40.80	356.54	21.18	0.02
64	279.28	−36.98	354.55	23.63	0.09
65	299.61	−35.57	350.84	24.28	0.15
66	392.20	−32.82	352.40	24.17	0.14
67	294.24	−26.91	342.72	24.41	0.20
68	543.24	−23.52	399.42	23.84	0.12
69	302.19	−22.53	337.63	23.17	0.05
70	526.34	−19.58	387.24	24.37	0.14
71	434.18	−12.27	342.59	23.97	0.20
72	305.98	−2.40	317.26	21.77	0.03
73	392.99	0.26	320.05	24.46	0.18
74	282.36	0.88	316.65	22.13	0.02
75	518.36	2.00	364.62	22.04	0.04
76	2.11	2.87	451.73	22.82	0.08
77	171.63	4.45	347.52	20.67	0.02
78	365.24	5.01	311.02	24.34	0.14
79	134.00	7.02	364.00	21.49	10.00
80	258.48	7.98	314.16	23.84	0.07

Table 9(cont.)

Star	X	Y	R	V	σ
81	81.42	9.96	392.47	19.60	0.01
82	224.05	14.38	317.66	22.48	0.09
83	487.72	15.94	337.37	23.15	0.03
84	193.87	18.06	325.58	21.39	0.03
85	109.77	21.48	365.92	23.45	0.21
86	100.69	23.63	369.75	17.49	0.02
87	486.94	23.99	329.91	21.69	0.02
88	205.95	36.28	304.00	22.73	0.07
89	418.53	39.50	288.52	22.47	0.04
90	437.58	40.30	294.20	24.31	0.19
91	306.81	40.69	274.24	23.91	0.12
92	2.07	42.80	425.25	22.80	0.08
93	330.15	43.92	270.06	23.13	0.07
94	336.56	46.28	267.79	18.94	0.02
95	427.57	46.63	284.72	21.75	0.03
96	484.47	48.17	307.62	23.20	0.05
97	160.16	50.63	313.17	21.69	0.03
98	448.73	53.70	286.24	23.64	0.14
99	251.14	55.82	269.83	23.55	0.12
100	485.12	57.50	299.93	23.46	0.07
101	293.86	58.53	257.94	17.79	0.03
102	336.95	59.11	254.98	24.01	0.09
103	279.44	62.60	256.34	24.08	0.09
104	428.67	62.97	269.84	23.90	0.11
105	308.22	64.62	250.28	24.09	0.10
106	44.25	74.87	372.31	21.79	0.02
107	338.98	77.57	236.59	22.28	0.04
108	457.25	79.55	266.92	21.40	0.10
109	371.83	79.93	237.82	20.26	0.02
110	1.94	80.94	402.10	17.73	0.02
111	457.39	81.62	265.17	23.11	0.41
112	400.93	81.69	242.99	23.19	0.07
113	526.53	82.09	304.21	21.18	0.03
114	300.03	82.75	233.12	21.74	0.16
115	364.38	84.62	231.98	24.10	0.12
116	206.74	85.73	259.23	21.74	0.03
117	200.00	90.36	258.48	22.03	0.03
118	503.38	91.09	282.61	23.58	0.11
119	280.34	91.27	228.10	20.02	0.01
120	47.05	96.09	356.83	23.32	0.15

Table 9(cont.)

Star	X	Y	R	V	σ
121	49.15	102.01	351.57	21.36	0.05
122	350.63	102.66	212.36	17.59	0.03
123	510.76	106.77	275.22	24.32	0.15
124	207.44	107.77	239.69	22.96	0.07
125	379.04	109.30	210.56	16.77	0.05
126	38.95	109.48	355.41	21.48	0.03
127	503.62	112.58	266.15	23.92	0.10
128	107.89	116.69	296.80	23.91	0.12
129	131.11	117.29	279.46	23.17	0.07
130	552.09	118.01	296.47	23.57	0.14
131	57.16	125.10	331.54	19.55	0.01
132	524.31	126.07	270.57	24.06	0.18
133	146.69	127.29	261.38	20.39	0.02
134	8.63	128.72	370.62	23.13	0.05
136	231.93	132.03	206.52	23.05	0.13
138	126.71	134.89	270.65	19.04	0.02
139	481.87	136.31	233.97	23.40	0.13
141	480.54	138.88	231.16	23.18	0.10
142	194.62	139.60	220.54	20.30	0.02
144	136.79	141.02	259.04	21.56	0.03
146	507.98	142.44	247.46	24.22	0.13
147	478.78	149.47	222.06	23.28	0.11
151	542.89	156.17	265.30	24.09	0.17
155	144.73	160.98	239.99	23.53	0.15
157	551.69	161.66	269.28	21.26	0.03
158	146.59	161.88	237.99	22.71	0.07
161	108.01	164.93	267.08	23.74	0.13
163	497.88	167.94	222.79	24.48	0.25
168	126.44	179.14	243.86	22.06	0.05
169	105.04	180.66	261.18	19.79	0.02
184	519.34	212.77	215.02	22.77	0.07
185	45.32	213.93	301.40	22.57	0.07
186	121.21	214.27	231.04	19.04	0.01
192	153.63	217.07	200.92	19.39	0.02
194	543.77	217.32	234.94	24.00	0.15
207	27.84	230.00	313.26	23.42	0.04
209	525.90	230.38	213.33	24.64	0.10
211	46.73	232.83	294.31	23.97	0.23
218	550.30	244.36	231.39	24.63	0.17
220	530.92	246.23	212.39	23.15	0.07

Table 9(cont.)

Star	X	Y	R	V	σ
224	536.03	253.48	215.08	23.24	0.07
230	537.03	261.37	213.97	24.69	0.19
237	558.03	270.25	232.55	24.71	0.25
257	57.11	293.81	273.27	21.70	0.02
258	79.50	294.97	250.85	23.85	0.17
264	551.04	310.34	221.44	24.87	0.18
276	27.05	325.14	302.79	23.46	0.12
277	554.15	326.88	224.89	21.78	0.03
316	9.44	371.45	325.31	23.87	0.14
318	118.72	373.31	219.10	23.50	0.12
319	137.03	375.17	202.09	23.36	0.09
325	91.67	379.12	246.71	23.59	0.16
327	9.19	382.08	327.60	21.56	0.03
329	30.30	383.47	307.29	23.20	0.08
346	10.87	399.74	330.10	22.25	0.10
347	71.71	403.79	273.11	23.82	0.16
354	536.15	410.18	227.83	20.57	0.02
361	122.41	416.61	231.24	23.22	0.08
363	159.07	421.34	201.54	22.46	0.04
364	72.00	422.59	279.59	22.87	0.07
365	83.16	424.42	270.08	23.22	0.07
366	126.82	425.92	231.65	22.12	0.04
371	84.58	432.86	272.36	23.13	0.09
377	490.23	443.81	206.51	24.46	0.10
381	515.73	446.26	228.32	23.58	0.07
382	503.98	447.09	219.35	24.13	0.11
383	156.51	447.24	218.47	23.60	0.13
386	162.47	453.92	218.00	23.99	0.22
396	557.29	472.13	277.20	21.60	0.03
397	482.84	475.89	222.91	24.04	0.08
398	62.42	477.40	313.22	22.77	0.05
402	499.84	485.22	241.44	24.50	0.13
407	167.86	495.05	242.81	23.67	0.12
409	481.68	495.50	236.79	22.79	0.07
410	90.13	499.73	303.09	22.21	0.04
411	416.67	500.39	205.73	23.39	0.08
413	449.42	501.97	222.91	24.61	0.10
414	403.19	512.24	211.47	24.70	0.20
415	432.31	515.11	225.82	22.07	0.02
416	322.54	516.49	202.63	24.91	0.23

Table 9(cont.)

Star	X	Y	R	V	σ
417	338.34	518.28	204.49	24.08	0.10
418	269.64	521.52	216.04	21.77	0.05
419	397.26	521.53	218.29	22.02	0.02
420	356.92	521.94	209.74	23.80	0.10
421	337.68	528.29	214.46	22.88	0.11
422	516.51	529.22	285.05	24.49	0.19
423	452.14	532.48	250.50	24.31	0.17
424	471.80	533.18	261.27	24.19	0.10
425	362.21	533.36	221.79	20.34	0.01
426	506.19	537.15	284.57	24.59	0.11
427	315.49	537.29	223.76	24.26	0.11
428	413.33	539.81	240.84	24.05	0.07
429	332.88	542.55	228.59	24.92	0.27
430	418.69	543.95	246.61	24.24	0.07
431	265.04	545.16	240.03	24.42	0.13
432	319.49	545.85	232.09	23.89	0.09
433	353.35	547.84	235.06	23.92	0.13
434	313.64	552.64	239.20	24.76	0.22
435	314.43	554.31	240.81	24.85	0.23
436	514.48	557.72	305.91	24.01	0.14
437	499.14	557.87	297.01	22.12	0.03
438	320.08	563.64	249.84	23.93	0.09
439	396.95	564.12	259.04	22.38	0.07
440	286.68	579.00	268.48	23.09	0.16
441	354.44	579.36	266.54	19.46	0.05
442	359.62	579.47	267.18	24.40	0.16
443	363.08	580.46	268.57	24.05	0.12
444	442.14	582.19	290.85	22.42	0.14
445	391.68	586.70	279.69	24.18	0.12
446	558.32	593.47	361.13	24.72	0.22
447	496.71	594.16	326.22	24.77	0.18
448	340.08	595.15	281.36	24.98	0.22
449	345.53	595.45	281.92	22.65	0.09
450	533.82	597.64	349.51	24.16	0.13
451	311.42	602.88	289.47	24.65	0.21
452	407.00	603.73	299.90	22.31	0.05
453	376.80	604.47	294.29	23.69	0.09
454	364.73	606.99	295.10	23.87	0.08
455	535.51	615.88	365.42	21.46	0.05
456	272.44	618.19	309.54	24.19	0.10

Table 9(cont.)

Star	X	Y	R	V	σ
457	548.73	618.89	375.47	24.97	0.16
458	336.42	620.50	306.60	24.73	0.17
459	348.15	621.15	307.73	24.93	0.14
460	411.35	621.42	318.12	24.25	0.18
461	503.64	626.84	358.00	24.60	0.20
462	525.27	627.69	369.71	24.45	0.19
463	559.89	629.18	390.35	22.75	0.14
464	558.61	629.78	390.08	23.54	0.40
465	332.68	640.62	326.65	24.17	0.12
466	308.38	648.78	335.47	24.48	0.17
467	366.19	653.39	341.37	24.57	0.15
468	406.14	662.82	357.13	24.73	0.11
469	504.82	664.14	391.54	24.77	0.22
470	554.15	664.78	416.50	24.92	0.47
471	341.29	674.54	360.75	20.17	0.02
472	493.63	677.63	398.92	24.57	0.14
473	432.64	677.96	378.28	24.96	0.18
474	409.47	686.59	381.07	23.87	0.11
475	376.86	692.76	381.71	20.18	0.04
476	549.22	695.20	439.94	24.66	0.24

Table 10
Photometry for BKGD SW

Star	X	Y	V	σ	Star	X	Y	V	σ
1	88.01	11.10	24.59	0.26	41	140.52	119.63	24.69	0.22
2	129.72	11.22	23.87	0.06	42	182.33	121.63	24.31	0.10
3	89.55	11.67	24.50	0.24	43	231.06	122.99	24.40	0.12
4	70.97	13.10	24.03	0.08	44	206.21	124.58	20.89	0.01
5	134.23	16.51	24.69	0.17	45	166.00	125.10	24.62	0.10
6	241.95	16.80	23.65	0.06	46	90.71	129.80	22.53	0.03
7	100.15	20.05	21.54	0.02	47	121.60	130.18	24.19	0.16
8	208.36	21.82	23.88	0.09	48	212.37	131.83	22.39	0.02
9	222.24	23.97	22.14	0.03	49	200.79	136.52	24.18	0.14
10	38.19	32.75	24.75	0.16	50	295.44	138.73	24.33	0.18
11	140.21	34.60	24.94	0.25	51	297.81	139.17	24.68	0.22
12	240.81	39.28	24.29	0.09	52	101.43	142.48	22.47	0.03
13	161.47	39.57	18.66	0.03	53	175.14	142.57	24.51	0.11
14	215.77	39.86	19.74	0.01	54	179.48	144.17	23.21	0.08
15	165.12	40.16	17.50	0.04	55	285.80	144.46	24.38	0.11
16	96.19	40.22	24.10	0.10	56	66.01	148.56	23.95	0.04
17	56.10	44.91	24.87	0.17	57	286.10	157.86	24.75	0.13
18	67.19	49.96	24.43	0.11	58	154.47	163.32	22.53	0.03
19	51.90	54.89	23.27	0.05	59	174.82	164.17	23.53	0.06
20	221.03	55.27	24.62	0.08	60	189.57	167.56	24.72	0.21
21	169.90	58.13	24.92	0.20	61	135.44	167.84	17.16	0.01
22	128.10	63.60	23.37	0.04	62	21.91	171.66	24.38	0.11
23	277.55	65.02	22.88	0.07	63	259.78	174.60	23.64	0.08
24	124.19	65.84	23.55	0.05	64	17.23	176.32	24.33	0.12
25	215.95	70.30	23.85	0.05	65	283.30	177.58	24.07	0.08
26	12.53	71.25	24.63	0.12	66	47.57	178.97	24.13	0.10
27	69.49	73.79	23.96	0.09	67	288.93	179.60	23.33	0.04
28	78.69	74.74	24.34	0.16	68	262.00	181.62	24.41	0.12
29	37.75	77.21	23.21	0.03	69	155.66	187.83	23.88	0.09
30	112.42	78.57	23.25	0.09	70	118.17	189.26	24.86	0.15
31	227.99	83.16	24.49	0.19	71	281.44	190.08	23.77	0.10
32	104.22	85.38	23.95	0.10	72	112.11	195.35	24.82	0.14
33	170.97	87.36	24.67	0.15	73	208.34	199.17	23.50	0.05
34	120.26	87.83	24.92	0.19	74	91.36	200.20	23.94	0.11
35	132.04	89.04	24.46	0.21	75	136.79	205.24	23.37	0.11
36	23.58	91.85	22.47	0.02	76	292.51	206.62	22.45	0.03
37	61.16	93.57	23.99	0.08	77	150.49	206.77	23.10	0.05
38	120.87	95.10	24.87	0.18	78	178.54	207.18	24.49	0.09
39	73.15	103.87	24.76	0.13	79	40.70	213.94	24.57	0.14
40	33.92	117.48	22.93	0.04	80	119.51	214.33	20.21	0.01

Table 10(cont.)

Star	X	Y	V	σ	Star	X	Y	V	σ
81	283.31	217.28	24.07	0.12	121	47.30	333.15	24.93	0.16
82	270.91	223.67	22.70	0.03	122	107.45	334.22	22.87	0.04
83	244.62	223.90	23.36	0.08	123	136.03	335.12	24.77	0.16
84	11.46	225.56	24.67	0.16	124	59.93	338.07	24.79	0.09
85	56.26	226.48	24.36	0.11	125	25.46	340.51	24.01	0.10
86	225.48	229.01	24.13	0.10	126	269.52	342.70	24.78	0.21
87	187.70	230.49	22.37	0.06	127	149.02	343.00	24.08	0.10
88	164.79	234.89	24.76	0.18	128	82.33	350.16	23.21	0.09
89	148.02	235.99	24.53	0.09	129	163.51	350.71	20.21	0.01
90	105.04	236.53	19.91	0.01	130	249.55	352.27	23.66	0.12
91	33.75	240.93	21.43	0.02	131	13.85	354.79	24.36	0.09
92	172.23	242.21	24.50	0.12	132	202.42	355.59	24.51	0.11
93	140.82	255.08	19.87	0.01	133	115.29	360.25	21.68	0.02
94	288.26	255.36	22.15	0.02	134	17.18	365.43	22.38	0.07
95	10.63	258.82	23.70	0.07	135	289.84	368.22	24.70	0.17
96	39.69	261.11	22.46	0.03	136	121.41	369.85	24.57	0.13
97	203.54	264.16	24.55	0.16	137	66.22	372.86	24.09	0.10
98	261.24	265.63	23.12	0.22	138	120.44	376.84	23.21	0.05
99	197.57	266.56	21.91	0.02	139	283.60	378.89	24.43	0.18
100	75.85	272.00	24.45	0.11	140	216.00	384.47	24.22	0.12
101	236.02	280.10	23.61	0.21	141	41.64	384.91	22.62	0.03
102	236.21	283.85	23.77	0.19	142	262.95	385.03	24.42	0.18
103	135.27	285.64	23.69	0.08	143	20.32	389.17	23.88	0.12
104	177.89	287.82	24.81	0.12	144	175.43	395.01	24.40	0.10
105	287.47	288.44	23.86	0.05	145	155.81	395.45	24.82	0.24
106	62.29	290.67	24.57	0.16	146	163.85	395.55	24.69	0.18
107	29.71	291.71	24.67	0.14	147	213.79	397.04	23.88	0.07
108	224.63	292.63	24.02	0.05	148	80.12	397.57	24.55	0.20
109	152.44	296.75	23.37	0.06	149	186.71	400.10	23.98	0.09
110	172.27	300.77	21.28	0.01	150	20.98	401.92	24.28	0.11
111	273.02	302.46	24.51	0.09	151	125.68	403.99	24.66	0.15
112	286.65	305.93	24.14	0.10	152	151.78	404.45	24.52	0.11
113	193.99	311.88	23.79	0.06	153	112.72	405.82	24.66	0.13
114	145.07	318.02	24.20	0.09	154	176.20	414.55	24.80	0.15
115	213.51	323.91	24.75	0.16	155	11.17	415.61	23.54	0.08
116	91.16	328.52	24.48	0.12	156	203.71	416.28	24.81	0.16
117	177.98	330.56	24.77	0.13	157	126.39	419.42	24.12	0.10
118	189.52	330.71	22.40	0.03	158	180.03	422.98	23.76	0.10
119	280.85	331.64	24.12	0.14	159	27.43	423.15	24.34	0.11
120	186.01	331.83	24.35	0.13	160	150.35	426.44	24.27	0.10

Table 10(cont.)

Star	X	Y	V	σ	Star	X	Y	V	σ
161	152.83	426.53	23.45	0.05	181	55.02	464.05	24.93	0.16
162	123.85	429.21	22.93	0.05	182	97.75	469.93	24.38	0.14
163	181.09	431.06	24.91	0.18	183	200.19	470.43	24.01	0.07
164	127.92	431.10	24.60	0.11	184	54.91	478.21	22.93	0.02
165	267.58	432.63	18.17	0.01	185	10.08	488.43	23.79	0.08
166	224.73	439.51	23.55	0.05	186	168.35	490.06	24.88	0.12
167	157.22	440.84	24.22	0.10	187	6.48	492.18	23.18	0.05
168	15.46	441.67	24.65	0.14	188	57.83	492.87	24.77	0.21
169	231.23	442.23	24.51	0.16	189	112.93	495.74	23.55	0.06
170	157.66	445.08	22.91	0.04	190	24.35	497.28	18.87	0.01
171	144.64	447.07	21.51	0.02	191	286.97	499.48	23.44	0.21
172	194.04	447.63	22.50	0.02	192	236.74	500.13	24.23	0.09
173	47.40	448.11	21.18	0.02	193	254.08	500.23	24.53	0.10
174	56.39	454.50	23.39	0.05	194	288.26	500.27	23.41	0.20
175	70.13	456.12	23.13	0.04	195	140.79	500.38	22.84	0.03
176	271.69	457.48	24.22	0.09	196	273.94	500.93	24.66	0.29
177	67.49	457.83	23.91	0.07	197	280.92	502.71	24.05	0.14
178	149.45	457.89	24.73	0.14	198	235.99	504.19	24.67	0.14
179	127.46	458.49	23.15	0.04	199	201.19	506.14	24.90	0.16
180	15.74	464.00	24.40	0.10					

Table 11
Photometry for BKGD NE

Star	X	Y	V	σ	Star	X	Y	V	σ
1	98.67	9.44	23.19	0.04	41	233.72	142.58	24.36	0.14
2	241.97	16.49	24.86	0.16	42	234.23	146.03	23.74	0.09
3	17.08	16.74	24.65	0.11	43	87.99	148.65	24.81	0.24
4	251.20	17.63	24.54	0.10	44	103.68	152.60	24.93	0.21
5	124.69	18.13	23.04	0.04	45	122.86	159.47	24.75	0.13
6	98.75	21.78	18.99	0.00	46	244.20	161.80	24.38	0.10
7	202.78	23.08	23.86	0.05	47	28.02	164.18	24.90	0.15
8	242.36	23.69	24.68	0.14	48	14.82	172.60	21.01	0.01
9	55.82	24.24	22.77	0.04	49	287.74	179.74	24.20	0.07
10	56.12	26.51	20.88	0.01	50	56.69	185.39	23.08	0.04
11	114.11	43.65	24.53	0.30	51	238.22	187.22	23.38	0.04
12	198.46	47.83	24.68	0.16	52	188.53	188.38	23.45	0.10
13	276.98	50.94	24.23	0.08	53	276.73	188.78	23.79	0.08
14	91.61	51.40	24.49	0.10	54	86.86	190.92	24.67	0.07
15	238.87	56.65	19.12	0.01	55	268.04	191.18	18.38	0.02
16	43.69	59.19	21.00	0.02	56	149.91	193.30	23.17	0.03
17	125.71	68.12	24.07	0.06	57	243.37	195.01	21.22	0.02
18	163.03	68.46	23.07	0.06	58	254.26	199.51	23.58	0.05
19	186.39	72.67	24.87	0.19	59	58.60	200.69	21.73	0.02
20	210.46	73.79	22.47	0.03	60	27.00	203.85	24.92	0.10
21	221.66	73.81	23.82	0.05	61	98.15	206.33	24.95	0.19
22	8.15	76.05	22.61	0.03	62	77.38	206.97	21.47	0.02
23	276.22	78.74	24.40	0.14	63	36.66	208.92	24.75	0.09
24	231.65	80.00	23.47	0.04	64	193.51	218.44	24.61	0.11
25	83.71	85.94	24.98	0.22	65	235.29	221.43	24.86	0.16
26	45.47	86.09	24.52	0.16	66	45.21	222.02	21.67	0.06
27	156.25	86.24	24.01	0.17	67	43.77	222.97	23.59	0.42
28	56.81	89.36	22.11	0.05	68	43.95	227.56	24.11	0.08
29	52.10	89.99	24.24	0.14	69	120.42	241.04	22.90	0.07
30	254.68	96.39	23.84	0.07	70	163.24	241.73	21.88	0.02
31	80.50	98.00	24.54	0.07	71	48.89	242.13	24.09	0.12
32	94.29	103.91	24.46	0.11	72	270.65	245.71	23.53	0.06
33	109.65	104.85	24.66	0.14	73	62.41	247.81	24.37	0.13
34	188.76	106.70	23.99	0.08	74	51.55	251.52	24.71	0.16
35	280.40	112.08	24.68	0.09	75	68.46	252.99	23.81	0.08
36	47.73	113.84	23.27	0.04	76	138.65	253.52	24.65	0.15
37	217.57	119.69	23.91	0.06	77	182.47	255.81	24.88	0.19
38	98.23	121.40	24.77	0.15	78	29.64	257.79	24.79	0.15
39	88.96	121.83	24.35	0.16	79	22.41	258.81	24.87	0.17
40	8.33	137.18	24.79	0.14	80	260.32	258.98	24.89	0.27

Table 11(cont.)

Star	X	Y	V	σ	Star	X	Y	V	σ
81	34.33	259.67	24.13	0.10	116	163.31	393.59	21.18	0.02
82	111.69	259.84	24.27	0.09	117	226.92	394.31	24.50	0.09
83	36.86	260.17	24.65	0.18	118	196.70	395.43	24.80	0.15
84	78.05	261.03	23.54	0.07	119	144.15	396.42	24.06	0.09
85	209.38	262.04	23.64	0.05	120	35.71	396.54	20.91	0.01
86	58.54	268.13	24.70	0.14	121	122.28	397.35	24.24	0.09
87	235.67	268.99	24.29	0.10	122	18.45	402.13	24.74	0.15
88	275.47	274.07	24.61	0.12	123	287.88	409.56	24.11	0.12
89	228.76	275.81	23.81	0.08	124	58.57	410.81	24.70	0.13
90	18.10	295.20	24.68	0.12	125	220.30	413.19	24.51	0.11
91	199.42	306.64	24.64	0.14	126	295.24	417.65	24.78	0.17
92	141.56	308.69	23.78	0.12	127	154.33	419.30	20.55	0.03
93	10.28	311.32	20.60	0.03	128	153.13	424.32	23.41	0.07
94	39.24	312.00	24.77	0.20	129	89.46	425.50	24.08	0.07
95	273.86	314.47	23.63	0.06	130	276.37	436.57	24.95	0.19
96	29.38	316.07	24.86	0.14	131	117.94	440.45	24.49	0.13
97	168.25	318.03	24.78	0.22	132	22.64	443.35	22.36	0.02
98	72.92	325.04	26.33	0.57	133	101.01	450.15	24.83	0.23
99	7.98	326.76	24.05	0.10	134	182.29	452.39	21.59	0.03
100	161.44	328.86	22.85	0.02	135	220.84	457.77	24.12	0.08
101	30.87	330.58	24.05	0.13	136	235.93	458.10	21.86	0.02
102	121.76	336.07	24.82	0.20	137	58.49	460.22	24.99	0.20
103	253.26	339.46	24.50	0.14	138	215.81	460.55	22.19	0.01
104	78.66	339.62	24.60	0.14	139	214.48	468.96	24.45	0.08
105	53.88	345.07	24.56	0.12	140	231.36	475.75	24.31	0.17
106	5.15	348.09	23.76	0.12	141	17.40	476.95	24.72	0.14
107	181.44	351.75	24.48	0.08	142	164.99	477.37	24.73	0.13
108	106.68	358.78	24.54	0.14	143	133.91	480.17	24.76	0.16
109	65.73	361.56	24.99	0.17	144	144.77	486.18	24.98	0.21
110	89.55	366.49	22.73	0.04	145	3.03	492.25	23.79	0.13
111	279.80	372.66	21.52	0.02	146	158.31	495.84	24.95	0.15
112	149.59	380.53	24.86	0.18	147	119.19	496.54	24.42	0.19
113	50.81	389.35	24.00	0.06	148	231.86	496.90	23.36	0.06
114	14.27	389.92	24.62	0.14	149	96.75	499.99	24.48	0.11
115	266.06	391.90	24.08	0.07					

IV. Luminosity Functions

It is now possible to construct complete luminosity functions for each of the frames. Fig. 5 shows the luminosity functions for both of the "background" frames (BKGD SW and BKGD NE) scaled to an area of 15.24 arcmin^2 (the total area of the CCD frames). The error bars are generated from the formula,

$$\sigma_n \approx \sqrt{\frac{n_{obs}}{f^2} + \frac{(1-f)n_{obs}^2}{n_{added}f^3}},$$

(Bolte 1988), where n_{obs} is the number of objects in the uncorrected bin, f is the ratio of *added* stars to *recovered* stars for each bin (the incompleteness factor), and n_{added} is the number of stars added to each bin, respectively. One can see that the shapes of the luminosity functions for the two corrected background frames agree at the 2σ level over the entire range of magnitudes, with the difference exceeding 1σ in five of the bins. For the rest of the analysis, the average of these two curves is used.

Fig. 6 shows the completeness-corrected luminosity functions for each of the three galaxy frames (GAL SW, GAL NW, GAL NE). Each plot contains three curves: the luminosity function for the region within two arcminutes of the galaxy centre (the Inner region); the luminosity function for the rest of the frame (the Outer region); and the average of the two background frame luminosity functions. The latter two have been scaled to the same area as the Inner region, and therefore the Y axis represents the true number of objects in the Inner region. The value of $2'$ ($\approx$ 18.3 kpc at D = 31.6 Mpc or 14.0 kpc at D = 24.0 Mpc) was chosen after an inspection of the star-lists, and roughly corresponds to the point where the density of objects reaches the background level. Credibility is lent to this claim from the fact that, for all three frames, there is excellent agreement between the luminosity functions of the Outer region of the background frames. This agreement

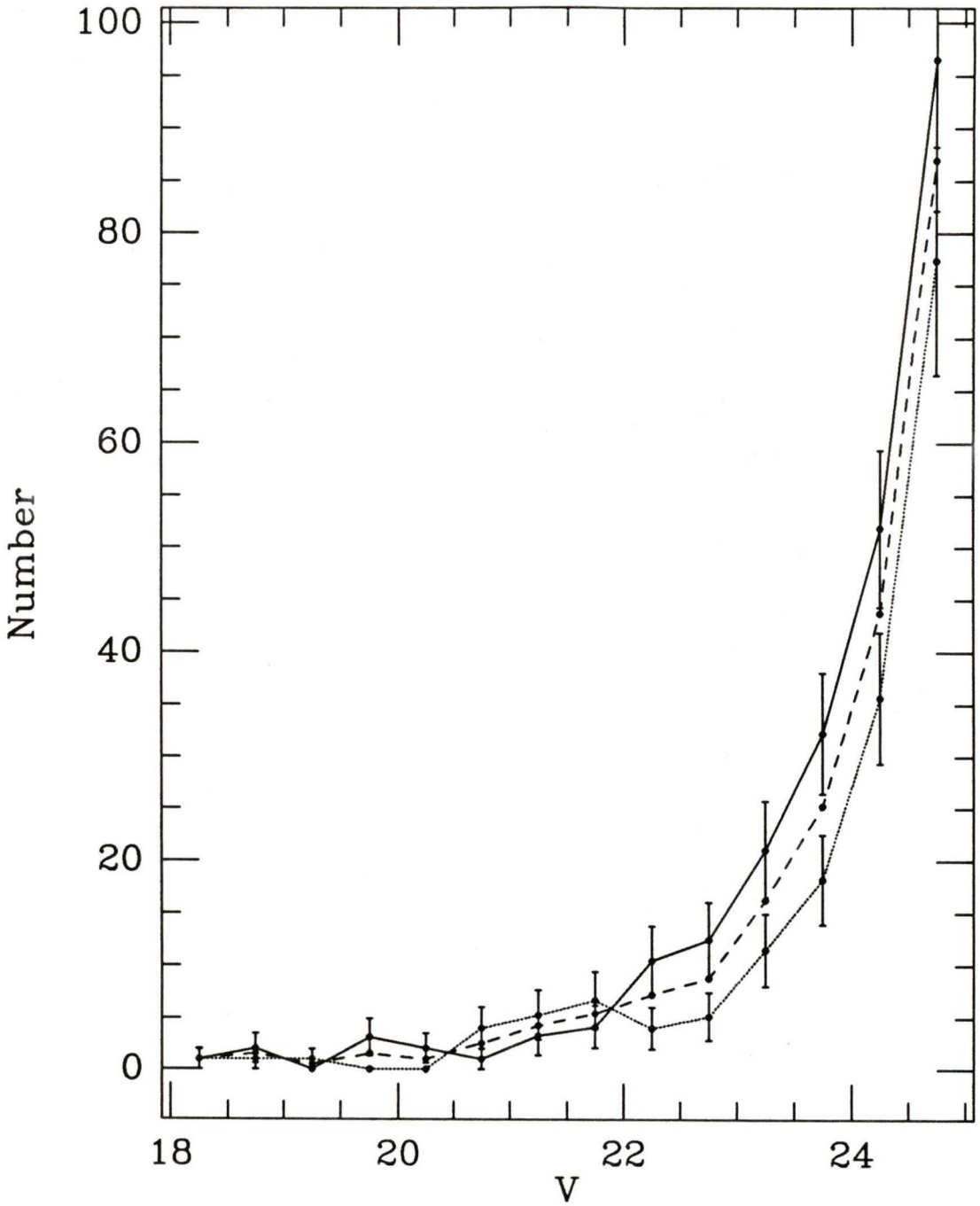

Fig. 5– Luminosity functions for BKGD SW (solid), BKGD NE (dotted), and the mean (dashed). For the sake of clarity error bars are not shown for the mean.

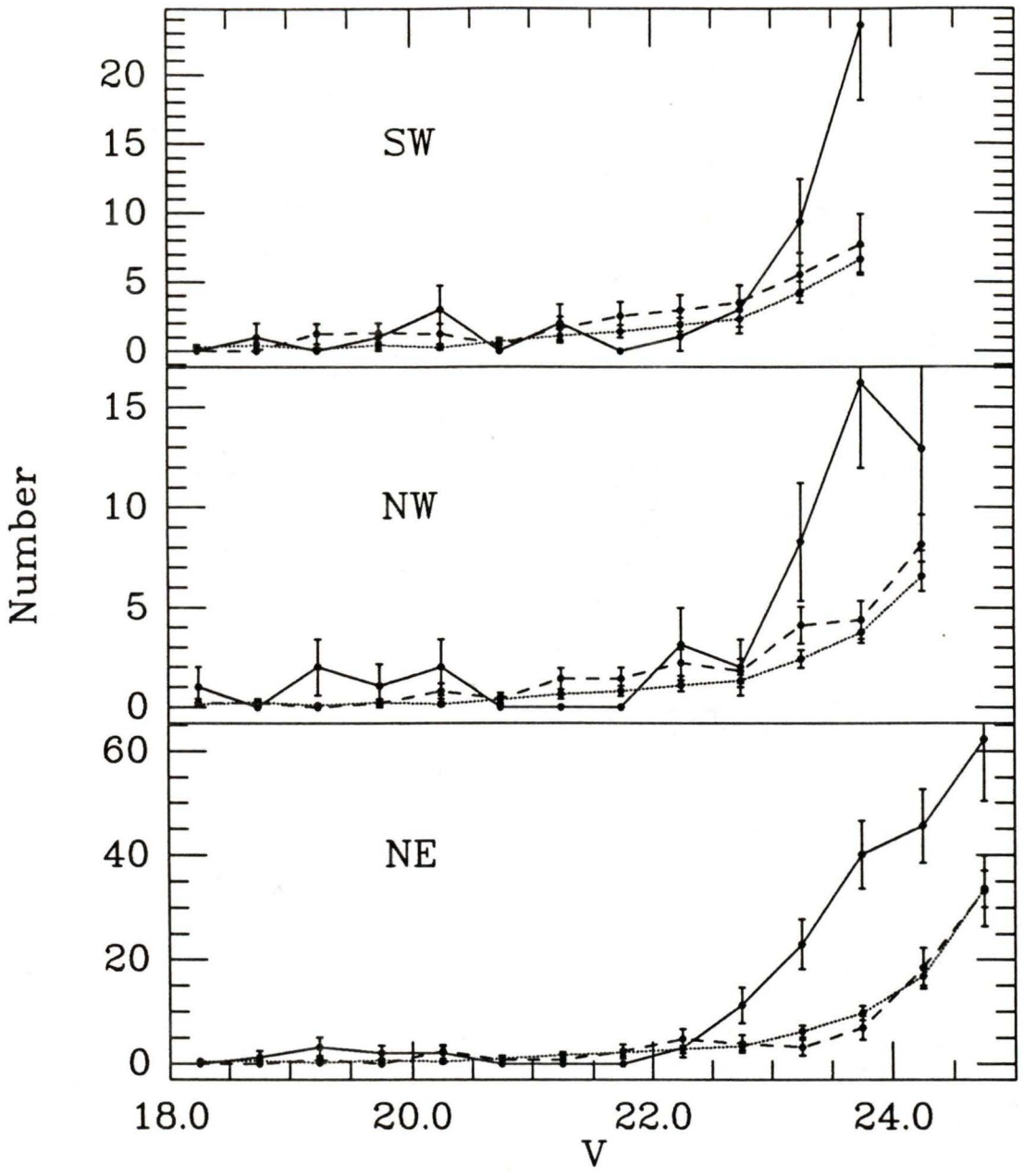

Fig. 6– Luminosity functions for the three galaxy frames. The solid line is for the Inner region, while the dashed and dotted lines are for the Outer regions and background scaled to the area of the Inner region, respectively.

also supports the success of the image classification in achieving a homogeneous background level on all the frames (see § III.B). Fig. 7 shows the background subtracted luminosity functions for all three galaxy frames. An excess of star-like images occurs in the Inner region of each frame, from which we quantitatively confirm the qualitative statement (c.f., H.C. Harris, Bothun, and Hesser 1988) that there has been a positive detection of a candidate cluster system.

Fig. 8 shows a superposition of the three galaxy frame luminosity functions scaled to the same area. There is excellent agreement for all three functions to 23.5 magnitudes (the level at which all three frames are complete to $\geq 68\%$). For the bin centred on V = 24.25 there is a suggested discrepancy between GAL NW and GAL NE, although they still agree at the rather large 1σ level. Perhaps the reason for this is that GAL NW has the smallest useable Inner region (2.28′ Table 2) of the three frames and is therefore more susceptible to small number statistics.

The final luminosity function is a combination of the three background-subtracted galaxy frames (Fig. 9). The total portion of the Inner area deemed useable is equal to 10.22 arcmin^2, or 81% of the inner 2′ . For V $\leq$ 23.5, the luminosity function is obtained by adding the three independent luminosity functions determinations. For the bin centred on V = 24.25, GAL NW and GAL NE are added together, and the value is scaled to the same total area as the brighter bins. Similarily, for the bin centred on 24.75, the GAL NE value is scaled (N.B.: objects common to more than one frame are counted only once).

V. Radial Number Density Distribution

A) Results

Despite the rather sparse data, and the large unuseable areas on the CCD, it is possible to examine the projected radial number density distribution of the

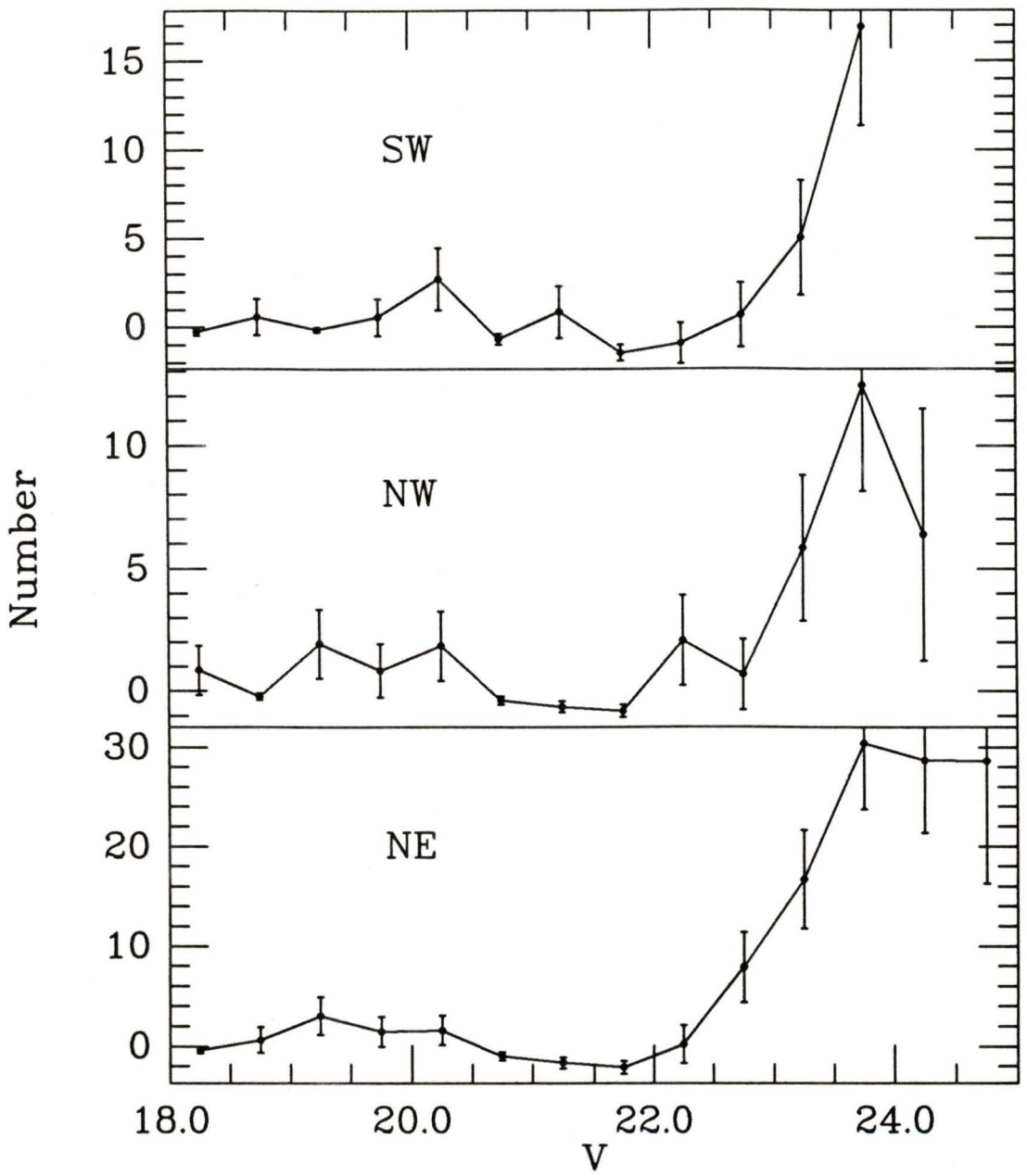

Fig. 7– The luminosity functions for the Inner areas of the three galaxy frames with the background subtracted.

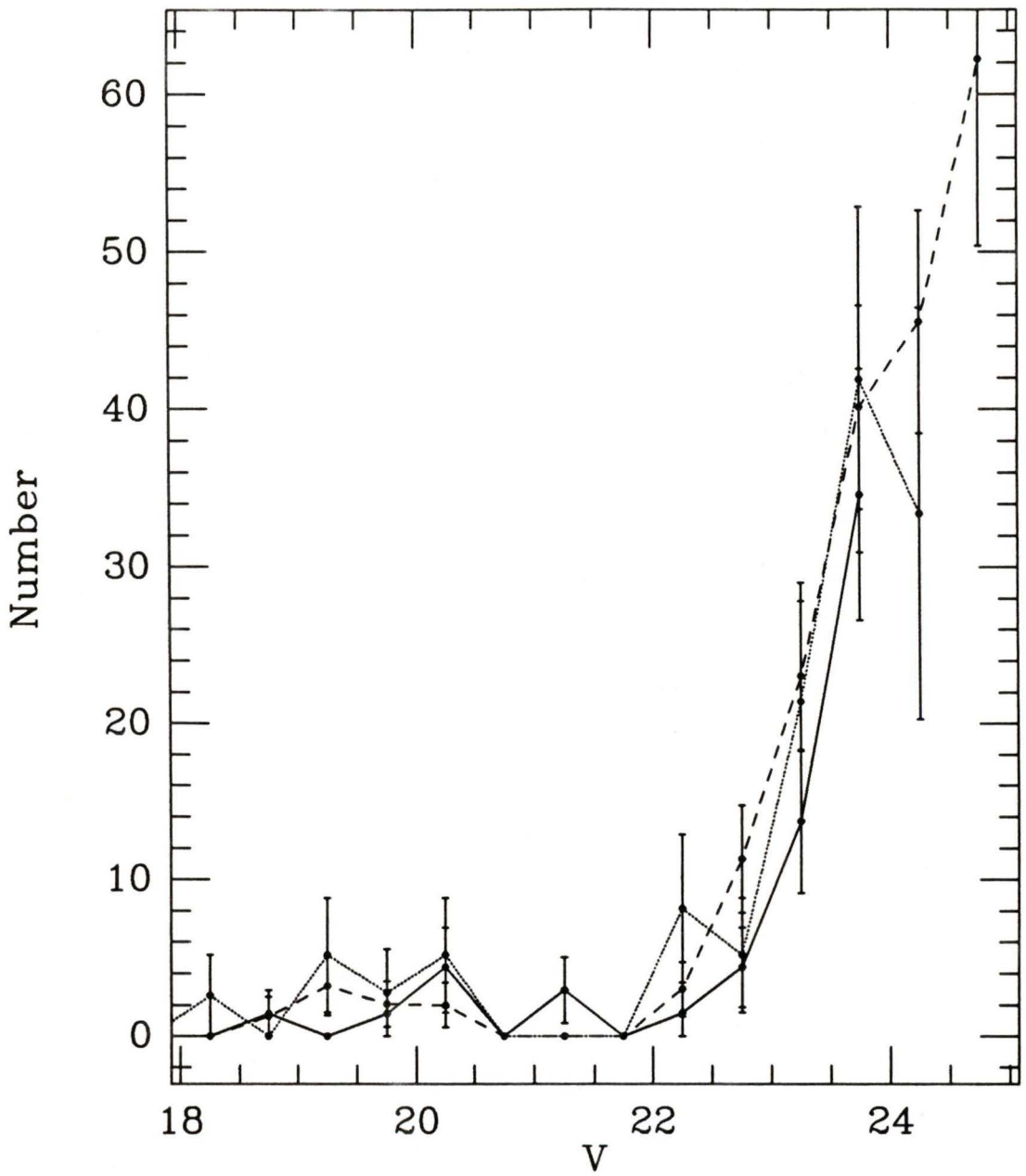

Fig. 8 – The three background-subtracted, luminosity functions scaled to the area of the Inner region of GAL NE (5.89 arcmin^2, see Table 2). The solid line is for GAL SW, the dotted line for GAL NW, and the dashed line is for GAL NE.

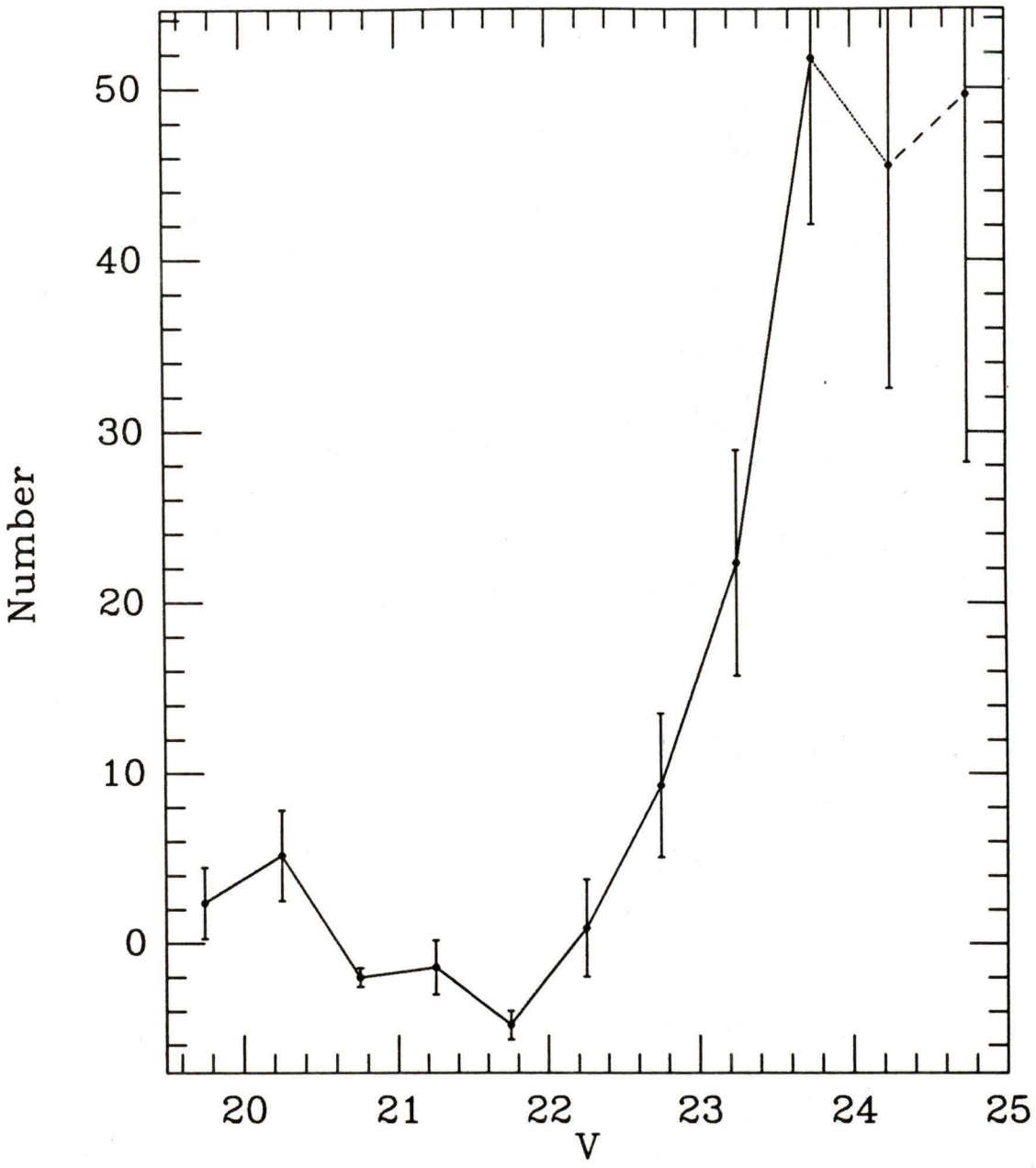

Fig. 9– The combined background-subtracted luminosity function for the region within 2′ of the galaxy centre. The second faintest bin is made up of GAL NW and GAL NE, while the faintest bin is only from GAL NE. They are both scaled to the same area as the other bins. The total area is 12.57 arcmin^2

presumed clusters. Due to different completeness limits on the frame, only the deepest frame was considered (GAL NE, see Table 7), and only the portion north-east of the galaxy was used owing to the large dust component on the south-west side. An appropriate background density was estimated as the average of the two completeness-corrected background frames ($V \leq 25.0$). This yields a background level of detections of 13.5 $\pm$ 0.8 arcmin^{-2}. Then the number density of objects was tabulated in concentric annuli about the galaxy centre (see Fig. 10). The centre radius of a given annulus is determined as the average radius of all the objects within the annulus. Table 12, column 1 shows the binned densities with the background level subtracted and their uncertainties. Columns 2 and 3 display the inner and outer radii of the given annulus. Columns 4 and 5 contain the mean distance to all the objects within each annulus and the total useable areas of the annuli, respectively.

Weighted least-squares solutions of the form,

$$Log(\sigma) = C_1 + C_2 Log(R), \quad \text{and}$$

$$Log(\sigma) = C_3 + C_4 R^{\frac{1}{4}},$$

were performed, where σ and R are given in Table 12. The coefficients thus derived are $C_1 = 1.28 \pm 0.07$ $C_2 = -1.69 \pm 0.24$, $C_3 = 4.36 \pm 0.42$, and $C_4 = -3.06 \pm 0.44$ ($R_e = 1.4'$) (See Fig. 11). The uncertainties cited here, are the formal errors of the fitting procedure, and reflect the errors in σ listed in Table 12.

B) Discussion

The most obvious parameter with which to compare the radial number density distributions of clusters is the galaxy light. It has been shown that the cluster number density distribution for NGC 4594 (an Sa galaxy; (c.f., Harris, Harris, and Harris 1984), scales similarly to its halo light, while for NGC 4486 (an E0

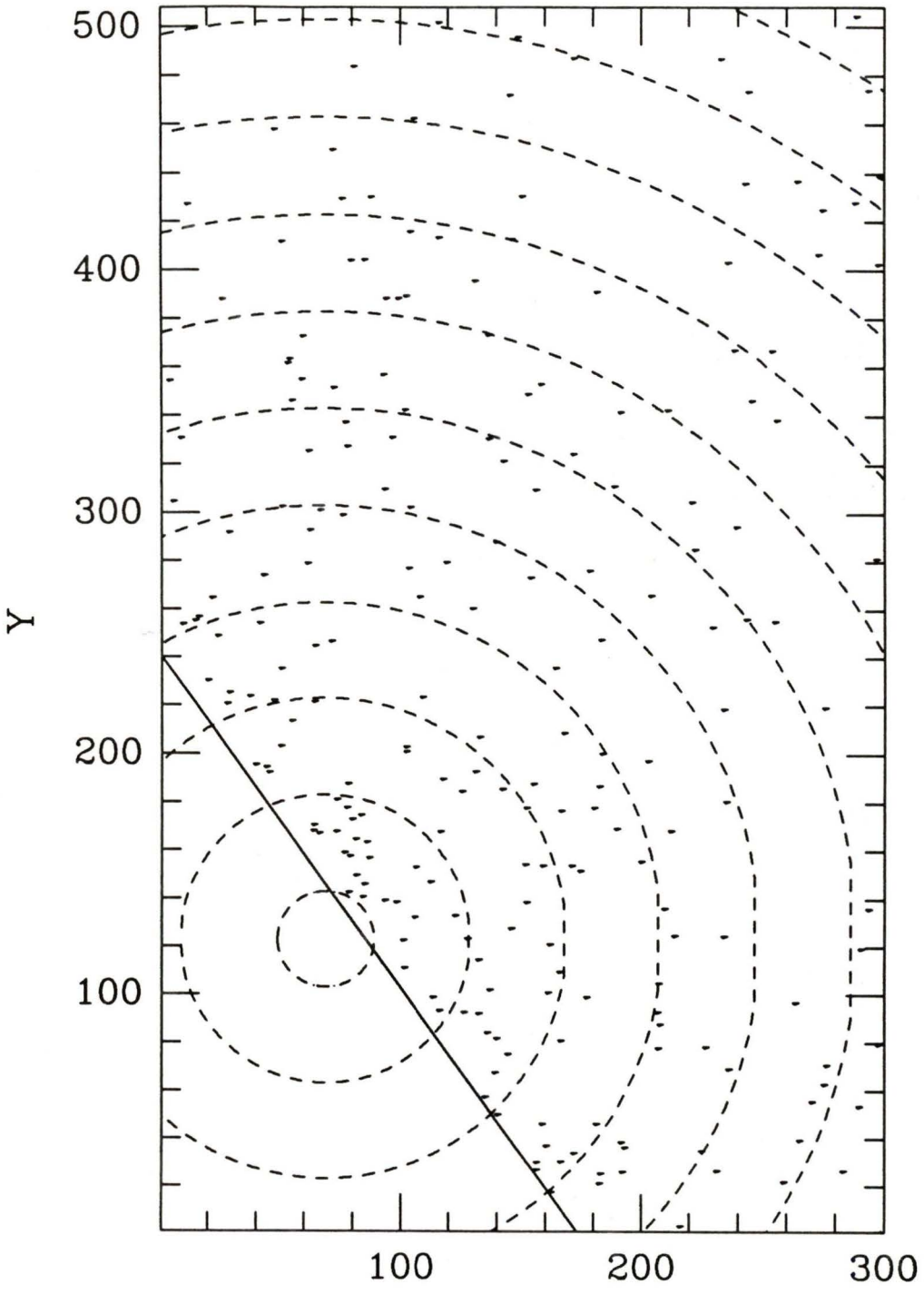

Fig. 10– The galaxy frame GAL NE with the annuli used to measure the radial density distribution. The solid line delineates the edge of the galaxy (i.e., the limit of the useable area), and the dashed lines are annuli spaced at 24″ .

Table 12

Background-Subtracted Radial Density Distribution for GAL NE

σ (arcmin^{-2})	R_i (arcmin)	R_o (arcmin)	$\langle R \rangle$ (arcmin)	Area (arcmin^2)
81.4 ± 16.7	0.2	0.6	0.423	0.339
26.1 ± 6.7	0.6	1.0	0.834	0.871
10.8 ± 4.0	1.0	1.4	1.202	1.528
11.3 ± 3.8	1.4	1.8	1.571	1.762
1.4 ± 2.7	1.8	2.2	2.029	2.007
3.9 ± 3.2	2.2	2.6	2.344	1.692
0.6 ± 3.3	2.6	3.0	2.817	1.322
–5.9 ± 2.4	3.0	3.4	3.170	1.270
–2.7 ± 3.0	3.4	3.8	3.617	1.237

galaxy; W.E. Harris 1988a), the clusters seem to form a more extended system than the halo light.

An attempt was made to measure the halo light distribution of NGC 5170. This was done using the galaxy-centred frame, GAL CV, that was star-subtracted and cosmetically repaired as explained in § III.E. The pixels were sampled in concentric annuli centred on the galaxy centre, in much the same way as the cluster counts were done. In an attempt to exclude disk and bulge light, all pixels within a distance of 0.20′ from the galactic plane, and the region within 1′ arcmin of the galactic centre, were excluded. The median of all the remaining pixels in each annulus was calculated and used to represent the luminosity of that annulus. Straight line fits to the scaled halo light distribution, can be seen as the dashed

lines in Fig. 11.

The frame used for this analysis is a short exposure (180 s), and the measurement was done in a rough manner; consequently there exists the possibility of some contamination from the disk and bulge, especially in the innermost regions. As well, the flat-fielding by dome flats is probably not as rigorous as is usual for surface photometry of extended objects. Therefore, the derived halo light distribution is at best approximate.

The straight line fits to both the cluster density distribution and the galaxy halo light, illustrated in Fig. 11, are in excellent agreement with one another. The two lines are virtually coincident for the power-law relation (upper part of Fig. 11), and are very similar in the case of the $R^{\frac{1}{4}}$ law (lower part of Fig. 11) with, perhaps, the clusters falling off slightly faster than the halo light. Within the errors, the halo light distribution and the cluster density distribution are consistent with one another, although the possibility still exists that more accurate surface photometry could reveal a systematic difference between the two.

Based on data from *elliptical* galaxies, Harris (1986) showed that the power law index describing the projected spatial distribution of globular clusters (C_2) scales with the total galaxy light according to

$$C_2 = -0.28 M_V^T - 7.9.$$

Qualitatively, this means that the brighter the galaxy, the less centrally concentrated are its globular clusters. Inserting $M_V = -22.0$ (§ III.E) yields $C_2 = -1.73$ which is consistent with the value of $C_2 = -1.69 \pm 0.24$, derived for NGC 5170. This suggests that the same power-law relation describes the NGC 5170 GCS, provided that the Fisher-Tully luminosity is used. Conversely, use of the Fisher-Tully luminosity is supported assuming that the power-law relation is valid.

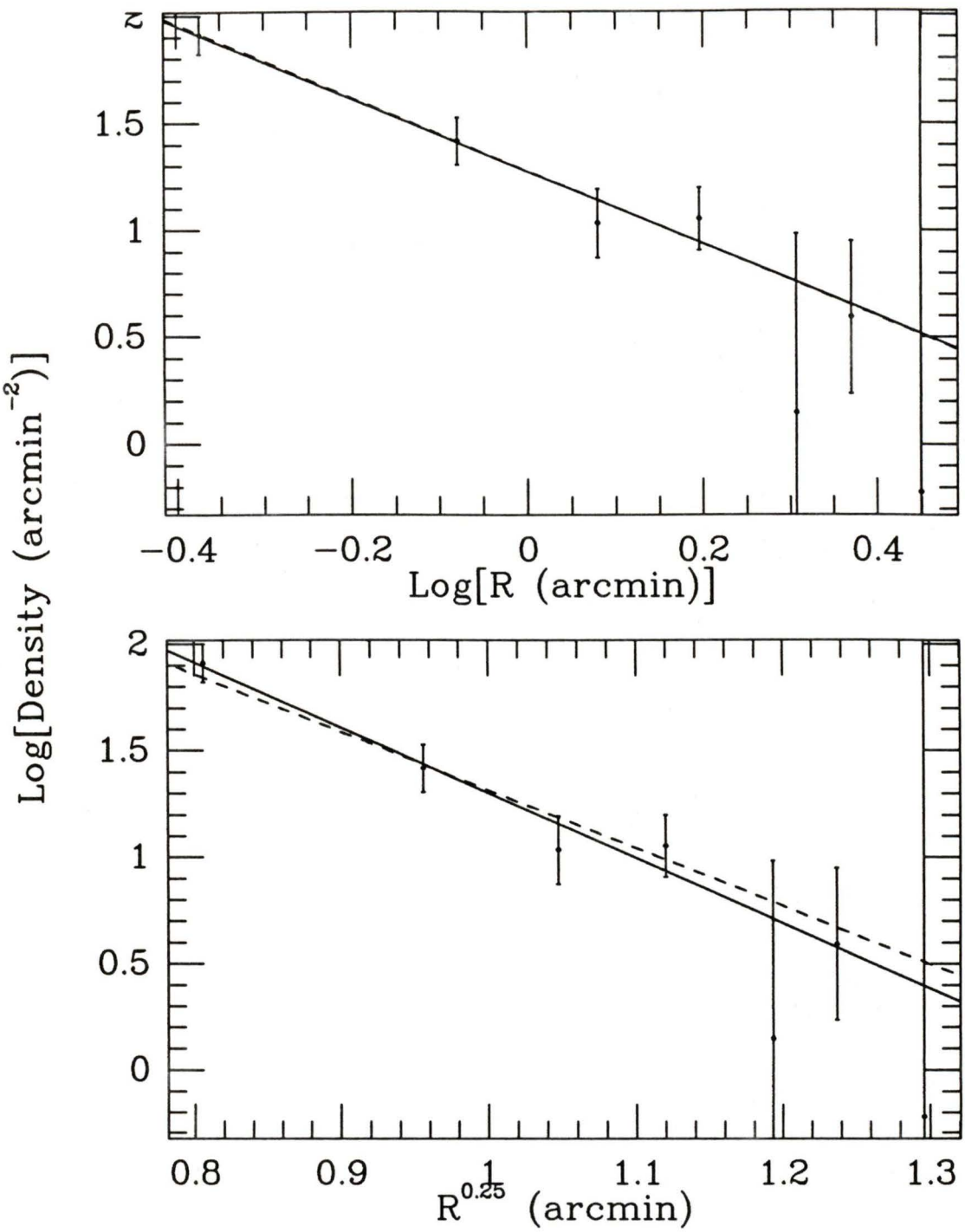

Fig. 11– Radial number density distributions for the globular clusters of NGC 5170. The solid lines are the fits to the cluster data (See text for slopes and intercepts) and the dashed lines represent the halo light.

Finally it should be noted that systematic errors may have been introduced into the radial number density determinations by a possible gradient in the completeness ratios as a function of R. One would expect that the completeness ratio at the faint end would be somewhat lower closer to the galaxy centre due to the higher level of noise present there. This has been compensated for, somewhat, by measuring separate completeness levels for Inner and Outer regions, resulting in average completeness levels for each region. In fact, even within the Inner region there probably exists a gradient in completeness such that the density values at smaller radii may have been underestimated, while at larger radii, they would have been overestimated. The net result is a possible overestimate of the power-law index; that is, the clusters may be seen to be less centrally concentrated than they really are.

VI. Distance Determination

A) Results

Although controversy has surrounded the use of globular cluster luminosity functions (GCLFs) as extragalactic distance indicators, W.E. Harris (1988b) has summarized current evidence favouring their application. The key assumption, based on empirical evidence, is that the luminosity function is, to first order, a gaussian distribution:

$$\phi(V) = Ae^{\frac{-(V-V_o)^2}{2\sigma^2}},$$

where A is a scale factor, V_o is the magnitude of the peak of the LF, and σ is the dispersion. It is necessary to make an assumption about the intrinsic value of M_{V_o}, thus making it possible to calculate the magnitude shift, and hence the distance modulus.

In the case of NGC 5170, the large error bars in the faintest bins of Fig. 9

render it difficult to determine whether the turn-over has been reached. As well, the luminosity function presented here is much sparser than those commonly found for the giant ellipticals generally used for this technique which often have more clusters in a single bin than the total number in the NGC 5170 LF. Therefore the distances derived here will have larger observational uncertainties than are usual for this method, independent of any problems inherent in the technique itself.

The first solution, using a weighted least-squares fit to the gaussian for the faintest six bins in Fig. 9 and allowing all three parameters to vary, yielded values of: A = 54.0 ± 9.0, V_o = 24.16 ± 0.23, and σ = 0.73 ± 0.21. The σ derived here is small compared to those typically found for other galaxies [generally $1.0 \leq \sigma \leq 1.5$ are obtained for local group galaxies (W.E. Harris 1988b)]. Doubtless, this is due the large errors in the the faintest two bins of the luminosity function, making the three-parameter fit a dubious prospect.

Hanes and Whittaker (1987) have demonstrated that reliable estimates of the turn-over luminosity can be obtained, even if one is considerably short of the turn-over magnitude, if the correct value of σ is adopted. Table 13 shows the results of weighted least-squares fits for different assumed values of σ. Columns 6, 7, and 8 will be discussed in the subsequent section. It can be seen from this table that as σ varies from 0.7 to 1.3 the magnitude of the peak of the GCLF (column 3) changes sytematically by about 1.2. This implies a corresponding change in the inferred distance modulus to the galaxy. If the GCLF is invariant among different galaxies then it seems justified to adopt the parameters derived from the Milky Way.

In order to achieve consistency, the Milky Way globular clusters were binned using the same magnitude bin width as was used for NGC 5170 (0.5 magnitudes). The values of M_V were taken from Webbink (1985). The gaussian fit yielded: A

Table 13

Gaussian Fits

σ	A	V_o	V_{ocor}	χ^2	M_V	N	S
0.5	57.7 ± 8.4	23.93 ± 0.09	23.76	4.6			
0.6	55.5 ± 8.3	24.01 ± 0.11	23.84	2.1			
0.7	54.4 ± 8.7	24.13 ± 0.13	23.96	1.3	–20.82	310 ± 90	1.45 ± 0.4
0.8	54.2 ± 9.4	24.26 ± 0.15	24.09	1.4	–20.95	350 ± 105	1.47 ± 0.4
0.9	55.2 ± 10.6	24.42 ± 0.18	24.25	2.1	–21.11	400 ± 125	1.45 ± 0.5
1.0	57.3 ± 12.3	24.61 ± 0.21	24.44	3.0	–21.30	480 ± 150	1.45 ± 0.5
1.1	60.9 ± 15.0	24.83 ± 0.24	24.66	3.9	–21.52	560 ± 190	1.38 ± 0.5
1.2	65.8 ± 18.0	25.06 ± 0.28	24.89	4.8	–21.75	660 ± 240	1.32 ± 0.5
1.3	72.3 ± 22.9	25.31 ± 0.32	25.14	5.5	–22.00	815 ± 320	1.30 ± 0.5
1.4	80.7 ± 28.9	25.58 ± 0.37	25.41	6.2			
1.5	91.3 ± 37.0	25.87 ± 0.42	25.70	6.8			

= 22.06 ± 0.57, M_{V_o} = –7.20 ± 0.04, σ = 1.28 ± 0.05 (see Appendix D). The values of M_{V_o} and σ are consistent with those used by others. For instance, Hanes and Whittaker (1987) find M_{V_o} = –7.1 ± 0.1 and σ = 1.15 ± 0.1, van den Bergh (1985) finds M_{V_o} = –7.11 ± 0.11 and σ = 1.35 ± 0.1, while W.E. Harris (1987) gives a value for M_{V_o} = –7.46 ± 0.28 based on globulars with 5 kpc ≤ R_{gc} ≤ 20 kpc. Therefore, fixing σ at 1.3, the value derived from the NGC 5170 data for V_o is 25.31 ± 0.32. Correcting for A_V = 0.17 gives a turn-over magnitude of 25.14. Using M_{V_o} = –7.20 yields a distance modulus of 32.3 ± 0.3. The error quoted here reflects only the formal error in the least-squares fit, which takes into account uncertainties in the luminosity function but not in the cluster photometry

(i.e., the photometry is considered to be perfect when the luminosity function is constructed), or errors in the parameters used, such as M_{V_o} or σ. Fig. 12 shows a plot of the luminosity function from Fig. 9, with two of the gaussian fits. The solid line is the three-parameter fit, while the dashed line has σ fixed at 1.30. It should be noted that if one decides to believe the three parameter fit a considerably closer distance modulus of 31.15 is implied.

B) Discussion

The only reliable distance available for comparison with the GCLF distance obtained above is from the Fisher-Tully (FT) relationship in H. As mentioned in § III.E, $(m-M)_H = 32.5 \pm 0.14$, which is within one standard deviation of the GCLF distance derived earlier adopting $\sigma = 1.30$. *This is the first direct comparison between these two techniques for the distance to a specific galaxy.* Other comparisons have been less direct, using distances derived to different galaxies in the same galaxy cluster. This can be problematic as the galaxies used for the GCLF technique are generally ellipticals located at the core of the cluster, while practitioners of the Fisher-Tully method use spirals located at large radii from the cluster centre and attempt to correct for back-to-front differences. The most studied galaxy cluster is Virgo, for which the latest GCLF distance modulus is 31.7 ± 0.22 (W.E. Harris 1988b), and the Fisher-Tully distance modulus is 30.96 $\pm$ 0.20 (Pierce and Tully 1988). It can be seen that, contrary to the result for NGC 5170, the FT and GCLF methods do not yield the same distance estimate to Virgo.

How reliable is the GCLF distance for NGC 5170? Unlike M 87 and other Virgo ellipticals, NGC 5170 is morphologically similar to the Milky Way, and therefore one feels a greater confidence in using the Milky Way parameters for

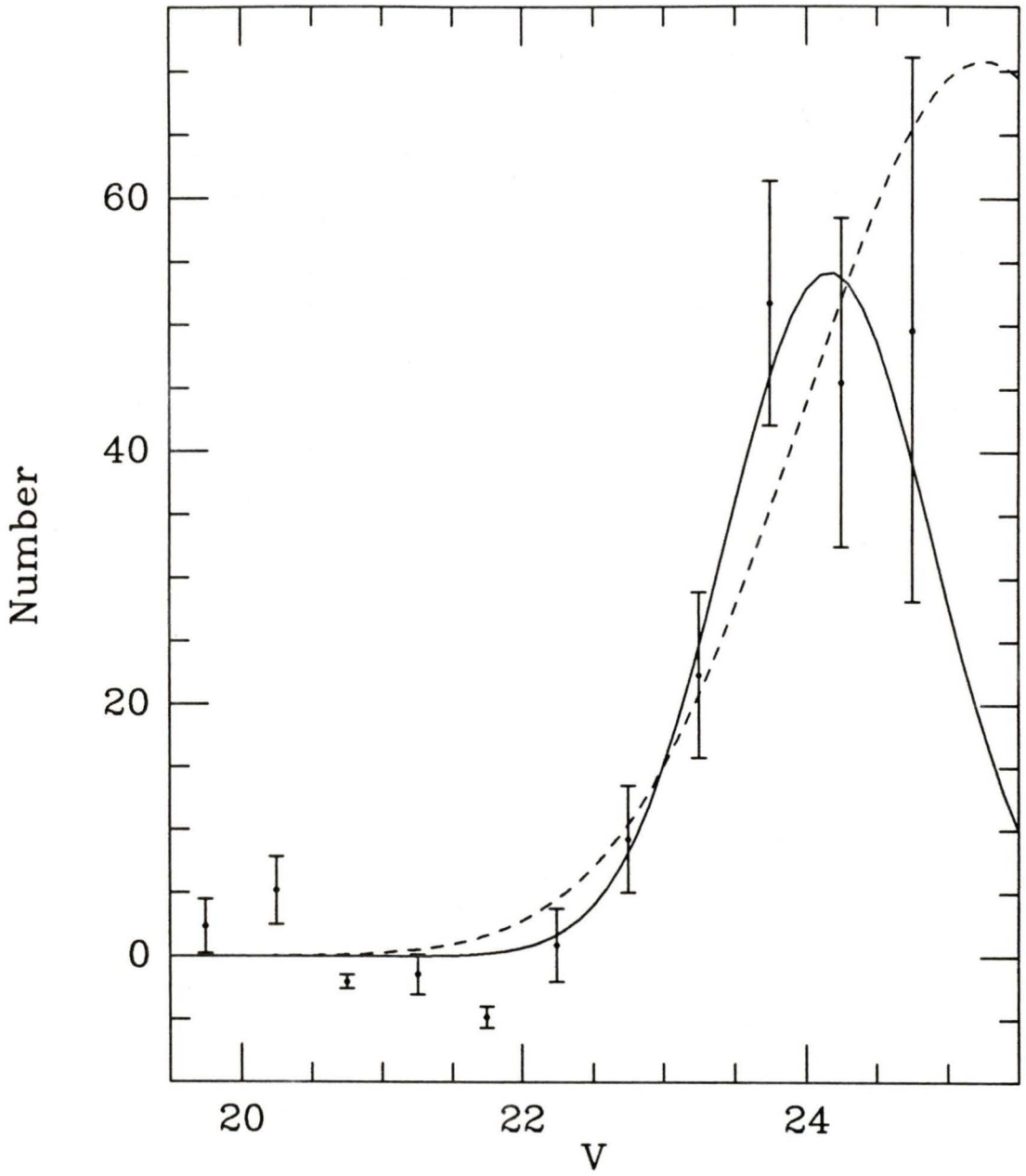

Fig. 12– The combined luminosity function as in Fig. 9, with two gaussians fit to it. The solid line is the three parameter fit, while the dashed line has assumed σ = 1.30, the value appropriate to the Milky Way GCS.

the comparison. On the negative side, NGC 5170 has a much higher intrinsic luminosity than the Milky Way [–22.0 vs. –20.6 (de Vaucouleurs and Pence 1978)]. W.E. Harris (1987) has shown that the dependence of M_{V_o} on intrinsic galaxy light, M_V^T, is not strong. But the relationship he finds,

$$M_{V_o} \propto (M_V^T)^{0.1},$$

is based on a study of only eight galaxies with large uncertainties in both M_{V_o} and M_V^T, resulting in a quoted error on the exponent of ± 0.07. Taken at face value, the above relationship would cause the NGC 5170 distance modulus to increase by about 0.15, thereby bringing the GCLF distance closer to the FT distance. It is important to remember that the total number of cluster detections for NGC 5170 is relatively small, and that the galaxy is very distant, resulting in the photometry falling short of the luminosity function peak. Deeper photometry would encompass the peak of the GCLF and thus add confidence to the derived distance and remove the neccessity for assuming a value of σ.

As a final note, recent work by Ciardullo, Jacoby, and Ford (1989), using planetary nebulae as distance indicators to galaxies in the Leo I group, has yielded a distance of 10.0 Mpc, which they claim is in close agreement with the FT distance (Pierce and Tully 1988), the luminosity fluctuation distance (Tonry and Schneider 1988), and the diameter-velocity-dispersion relationship (Davies *et al.* 1987; Burstein *et al.* 1987; and Dressler 1987). There is, however, a significant discrepancy between this distance and the GCLF distance of 6.8 ± 0.8 Mpc obtained by Pritchet and van den Bergh (1985) for NGC 3379, an E0 galaxy. This GCLF result is based on data which extends past the peak luminosity, but which includes only about 40 detected clusters. The planetary nebula provide a direct galaxy-to-galaxy comparison for all of the techniques (except FT), and, therefore,

ambiguity in galaxy location with respect to the cluster core is not a factor as it is with the Virgo results. The agreement of the above distance indicators, coupled with the fact that the shape of the planetary nebula luminosity function has a sound theoretical grounding (Jacoby 1989), suggests that the universality of the GCLF turn-over must be brought into serious question, although, as has been mentioned, the cluster sample size is very small for NGC 3379. Nevertheless, it has already been shown (W.E. Harris 1988b), that the GCLFs of several Virgo ellipticals seem to have dispersions which differ from the Local Group galaxies, and therefore it is not unreasonable to believe that peak luminosities can be different as well. The GCLF technique could possibly be convincingly tested, however, if the variation of the peak magnitude with galaxy morphological type, and intrinsic luminosity could be characterized theoretically and/or observationally. This might be achieved by observing a variety of galaxies within a given cluster.

VII. Specific Frequency

A) Results

In order to compare globular cluster systems of galaxies differing greatly in intrinsic luminosity, the concept of specific frequency, S, was developed by W.E. Harris and van den Bergh (1981). It is given by the formula,

$$S = N10^{0.4(M_V+15)},$$

where S is the total cluster population normalized to a galaxy luminosity of $M_V = -15$, N is the number of clusters belonging to the galaxy, and M_V is the galaxy luminosity. Before the specific frequency for NGC 5170 can be estimated, it is necessary to correct for the number of clusters which were missed in the analysis.

i. Superposition of Galactic Globular Clusters

The first way in which the number of missing clusters was estimated was to project the Galactic globular clusters on to NGC 5170 (see H.C. Harris *et al.* 1985, for a similar application to NGC 2683), and determine the number of these which would have been within the area surveyed and above the limiting magnitude of our data. This has been carried out for two separate distances (see § III.E), 31.6 Mpc (Fisher-Tully) and 24 Mpc (radial velocity). In this way, the inherent sensitivity of the technique to assumed distance can be evaluated.

Assuming the Fisher-Tully distance (which is similar to the GCLF distance, see § VI.A) of 31.6 Mpc and adapting Galactic globular cluster coordinates from Webbink (1986), the number of objects that would have been recovered is 15 out of 148 once $A_V = 0.17$ is taken into consideration. Integrating the luminosity function of Fig. 12 over a range of approximately four magnitudes on either side of the peak yields a total of 179 ± 28 clusters. Scaling by 148/15 gives 1770 ± 270 clusters for NGC 5170. Using M_V of –22.0 gives a specific frequency of 2.73 ± 0.43.

The second distance used was the radial velocity distance of 24 Mpc (m–M = 31.9) (see § III.E). The apparent magnitude of the galaxy is held at the same value as used above, meaning that M_V becomes –21.4. This time 31 out of 148 Galactic globular clusters would have been recovered (see Fig. 13), from which 860 ± 140 clusters are estimated. Proceeding as above, the resulting specific frequency is 2.36 ± 0.37. The errors quoted for both analyses result exclusively from the uncertainties in the luminosity function of the NGC 5170 clusters. That is, they result from contributions from variations in the background counts, inaccuracies in the completeness corrections, and binning statistics. Any differences in spatial distributions between the NGC 5170 and the Milky Way clusters have not been accounted for.

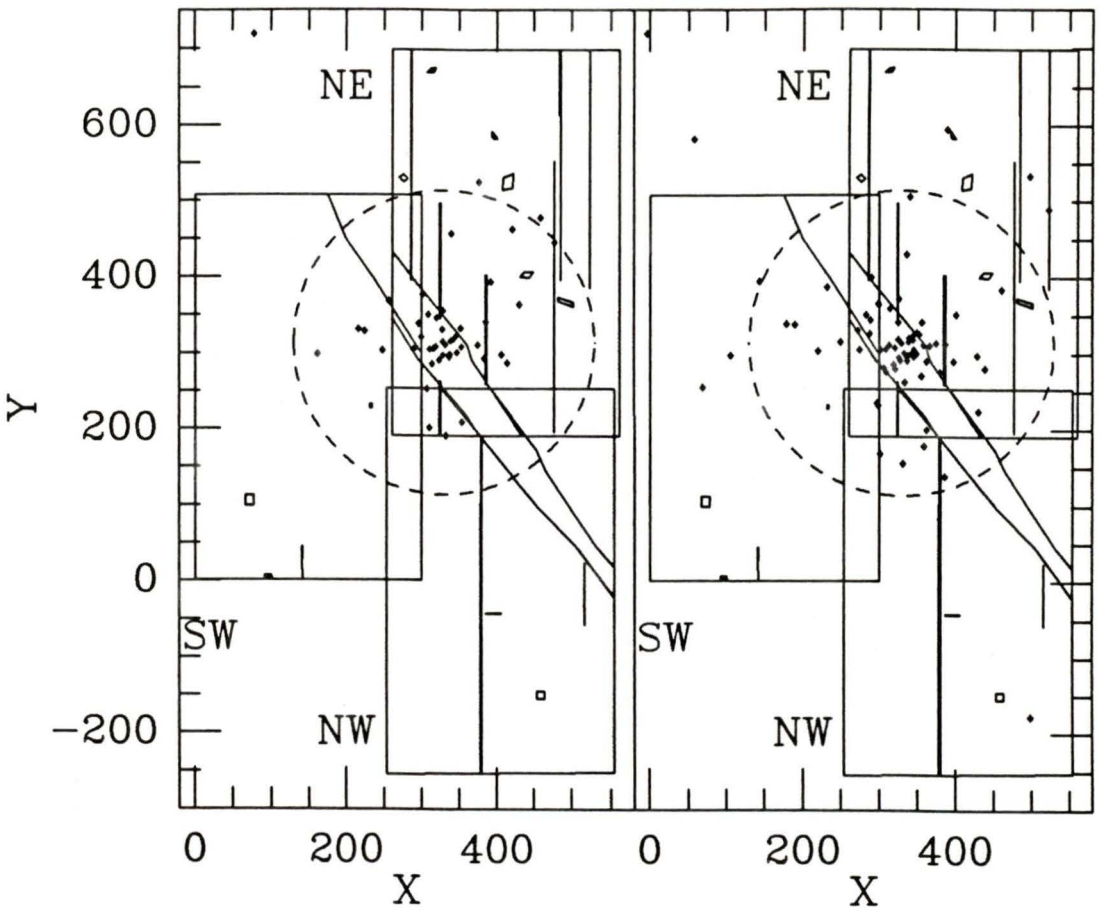

Fig. 13– Galactic globular clusters superimposed on NGC 5170 assuming a cut-off magnitude of V = 24.83. The figure on the left is for D = 31.6 Mpc and the on the right, D = 24 Mpc.

ii. Radial Density Extrapolation

An alternative method for estimating the number of globular clusters missed in our analysis is through the use of the radial number density function (to fill in the areas that could not be measured) and the GCLF (to fill in the clusters too faint to measure). The density function was derived in § V.A in two forms: as a power law, and as a de Vaucouleurs $R^{\frac{1}{4}}$ law. The $R^{\frac{1}{4}}$ law is favoured in this application as it has a faster drop-off at large R and is therefore probably a better representation of the cluster density distribution. Using this relationship with the coefficients derived in § V.A yields a total of 280 ± 40 clusters for $0.20' \leq R \leq 3.0'$. This corresponds to the range for which data were available, and for which there was an excess of counts above "background" (see Table 12). The problem now arises as to how far to extrapolate the relationship outwards and inwards to obtain an estimate of the total GCS. For $R \geq 3'$ it can be seen from Table 12 that there are actually fewer counts than would be expected from a pure "background", and therefore there is probably not a significant number of clusters this far out. Therefore 3′ (R ≈ 28 kpc for D = 31.6 Mpc or R ≈ 21 kpc for D = 24 Mpc) is a reasonable outer limit. Within 0.2′, however, a high cluster density is expected. Assuming D = 31.6 Mpc, the equivalent region in the Milky Way contains roughly 30% of the total globular clusters (it is lower for D = 24 Mpc). This percentage is probably somewhat lower for NGC 5170, as its clusters appear to be somewhat less centrally concentrated than the Galactic clusters (see § V.A), but it is likely still significant. A straight extrapolation of the radial density distribution to the galaxy centre will overestimate the total number of clusters in the innermost region due to the destructive effects of dynamical friction (Tremaine, Ostriker, and Spitzer 1975; and van den Bergh, Hesser, and Harris 1981). With this caveat in mind,

the observed radial density relationship was extrapolated to 0.1 arcmin, thereby adding about 30 ± 30 clusters. The remaining region has a linear radius of about 900 pc. For our galaxy, roughly 10% of the clusters are located within this radius, so 10% serves as an upper limit to the fraction of clusters missed for NGC 5170. The total number of clusters to a limiting magnitude of 25.0 is therefore 310 ± 50 clusters.

It is now neccessary to compensate for clusters missed due to their intrinsic faintness. To do this, a gaussian shape is assumed for the luminosity function, A = 72.3 ± 23, V_o = 25.31 ± 0.32, and σ = 1.30 (see § VI.A). Using this distribution to generate the entire luminosity function (i.e., to values of V such that $\phi(V) < 0.5$), gives a total of 470 ± 150 clusters. Since the scaled luminosity function of Fig. 9 contains 180 ± 30 clusters, we must multiply the total of V ≤ 25.0 by 2.61 ± 0.9 for a grand total of 815 ± 320 clusters. Using M_V = –22.0 for the galaxy yields S = 1.3 ± 0.5. The errors quoted here are due to the uncertainties in both the total number of found clusters (see above), and also the error in the gaussian fit to the luminosity function. The potential for missed clusters in the innermost 0.1 arcmin, has not been accounted for, but is expected to add less than 10% to S.

This technique yields S values which are fairly independent of the assumed distance to NGC 5170. Table 13 shows how S varies with σ of the GCLF. Column 6 contains the inferred absolute V magnitude of the galaxy (assumed to be 22.0 at D = 31.6 Mpc, see § II.E), while columns 7 and 8 show the total number of clusters and S, respectively. As σ varies from 0.7 to 1.3 the distance to the galaxy changes from approximately 17 Mpc to 31.6 Mpc, yet S only changes by about 10%, testifying to the robust nature of the above described technique.

B) Discussion

Firstly, it is worth discussing the relative merits of the two techniques used. Since both the Milky Way and NGC 5170 have similar morphological types, superposition seems, at first glance, reasonable. However, according to W.E. Harris (1986) and § V.B, bright galaxies tend to have their globular clusters less centrally concentrated than fainter galaxies. This could mean that the number of clusters missed in NGC 5170 is somewhat smaller than was derived above, leading to an overestimate of the specific frequency. The technique based on the measured radial distribution should circumvent this difficulty, and indeed does yield a lower value of S, but assumptions required to estimate the number of clusters hidden from detection in the galaxy centre limit its accuracy, as may the assumption of a gaussian form for the GCLF. Even assuming the gaussian does provide a good model, as evidence suggests, the fit used here is based on very sparse data, and this results in the derived parameters having large errors. Despite this, S = 1.3 ± 0.5 (perhaps slightly underestimated) is probably the best value of the three. It makes no assumption about the distance to NGC 5170 and it uses the Fisher-Tully luminosity (which is supported by the power-law index of the radial density distribution § V.A).

Exactly which intrinsic galaxy parameters would form the most informative comparisons to the cluster population is still in doubt. Comparing to the total galaxy light, as has been done here, seems logical, as this light should be representative of the total galaxy mass. However, globular clusters, being Population II objects, perhaps invite comparison to just the Population II light (i.e. halo and bulge). To this end, it is possible to make a rough approximation of the spheroidal light. The typical bulge-to-disk light ratio for an Sb galaxy is roughly 0.5 ± 0.2 (de Vaucouleurs 1977). Therefore $M_{V\,sph} \approx -20.8$, and $S_{sph} \approx 3.9 \pm 1.5$. The quoted error is underestimated in that it assumes that $M_{V\,sph}$ is exact.

The currently available data set for specific frequencies of spiral galaxies is very small. W.E. Harris (1988a) reviewed six disk systems, ranging from S0 to Sbc and gave S values as functions of spheroidal luminosity (bulge and halo, excluding the disk, see Table 14). As well, Blecha (1988), obtained S = 3.08 based on total galaxy luminosity for the Sb spiral NGC 3109 although an examination of his numbers failed to yield the same result as he obtained (and it will not therefore be considered further). All these studies are based on photographic data, and yield $\langle S_{sph} \rangle \approx 2.4$, consistent with the value obtained for NGC 5170. So far there do not appear to be any obvious trends for S with the parent galaxy luminosity. As more data are added from this project (see H.C. Harris, Bothun, and Hesser 1988) perhaps some trends will become evident.

Table 14

Specific Frequencies of Spiral Galaxies

Galaxy	Type	$M_{V\,sph}$	S^*_{sph}
Milky Way	Sbc	–19.8	2.2 ± 0.5
NGC 224	Sb	–19.6	4.5 ± 1.5
NGC 2683	Sb	–18.9	8.0 ± 4.0
NGC 3115	S0	–21.2	2.0 ± 0.5
NGC 4565	Sb	–21.4	1.0 ± 0.5
NGC 4594	Sa	–22.1	3.0 ± 0.3
NGC 5170	Sb	–20.8	3.9 ± 1.5

Note: The Spheroidal luminosities are generally poorly determined

Chapter 3

Conclusion and Future Work

1) The GCS of NGC 5170 has been detected as a significant excess of counts above "background" levels within 2′ of the galaxy centre.

2) The radial density distribution for NGC 5170 clusters agrees with results found for other galaxies, in that it exhibits a power-law index (-1.69 ± 0.24) consistent with its luminosity. Preliminary results indicate that there is relatively good agreement between the galaxy halo light and cluster radial number density, but better galaxy surface photometry is still required.

3) This is the first direct comparison between Fisher-Tully and GCLF distance determinations. Despite a relatively small total number of detected clusters, the agreement between the two techniques is quite encouraging, with the GCLF yielding 32.3 ± 0.30 vesus 32.5 ± 0.14 for the Fisher-Tully relation in H. A better understanding of how the turn-over luminosity varies with galaxy luminosity and morphology could potentially improve GCLF distance determinations. Confidence in the GCLF distance would have been higher had the turn-over been reached (the photometry was about 0.25 mag short of the turn-over).

4) The total size of the GCS is estimated to be 815 ± 300, yielding $S = 1.3 \pm 0.5$ based on total galaxy luminosity ($S_{sph} = 3.9 \pm 1.5$) which is consistent with S values found by others for isolated disk galaxies. The statistics are still too small for spiral galaxies to look for trends in S with various components of the galaxy light.

5) Similar observations to NGC 5170 have been made for six other disk systems. They will be reduced in a similar manner, and at that point it should be possible to comment on systematic differences between Fisher-Tully and GCLF

distances, and to see if there exist relationships between galaxy luminosity and S for disk galaxies. As the data set for all galaxy luminosities and morphological types increases in size, the relationship between GCS and parent galaxy characteristics should provide invaluable constraints on the earliest stage of galaxy formation.

References

Blecha, A. 1988, in *Globular Cluster Systems in Galaxies (IAU Symposium No. 126)*, eds. J.E. Grindlay and A.G.D. Philip, (Dordrecht: Reidel), p. 543 .

Bolte, M. 1988, DAO preprint: Mass segregation in the Globular Cluster M30.

Burstein, D., Davies, R.L., Dressler, A., Faber, S.M., Stone, R.P.S., Lynden-Bell, D., Terlevich, R.J., and Wegner, G. 1987, *Ap.J.Suppl.*, **64**, 601.

Ciardullo, R., Jacoby, G.H., and Ford, H.C. 1989, NOAO preprint No. 255.

de Vaucouleurs, G. 1948, *Ann. Astrophys.*, **11**, 247.

de Vaucouleurs, G., de Vaucouleurs, H., and Corwin, H.G. 1976. in *Second Reference Catalog of Bright Galaxies* (University of Texas, Austin), p. 194.

de Vaucouleurs, G. 1977, in *The Evolution of Galaxies and Stellar Populations*, eds. B.M. Tinsley and R.B. Larson, (Yale University Observatory, Connecticut), p. 43.

de Vaucouleurs, G., and Pence W.D. 1978, *A.J.*, **83**, 1163.

Dressler, A. 1987, *Ap.J.*, **317**, 1.

Davies, R.L., Burstein, D., Dressler, A., Faber, S.M., Lynden-Bell, D., Terlevich, R.J., and Wegner, G. 1987, *Ap.J.Suppl.*, **64**, 581.

Eastmond, T.S. 1977, Ph.D. dissertation, University of California, Los Angeles.

Eastmond, T.S., and Abell, G.O. 1978, *Pub. Astron. Soc. Pac.*, **90**, 367.

Graham, J.A. 1982, *Pub. Astron. Soc. Pac.*, **94**, 244.

Hanes, D.A. 1977, *Mem. R. astr. Soc.*, **84**, 45.

Hanes, D.A., and Whittaker, D.G. 1987, *A.J.*, **94**, 906.

Harris, H.C., Bothun, G.D., and Hesser, J.E. 1988, in *Globular Cluster Systems in Galaxies (IAU Symposium No. 126)*, eds. J.E. Grindlay and A.G.D. Philip,

(Dordrecht: Reidel), p. 613.

Harris, H.C., Hesser, J.E., Bothun, G.D., Hanes, D.A., and Harris, W.E. 1985, *A.J.*, **90**, 2495.

Harris, W.E., and van den Bergh, S. 1981, *A.J.*, **86**, 1627.

Harris, W.E., Harris, H.C., and Harris, G.L.H. 1984, *A.J.*, **89**, 216.

Harris, W.E. 1986, *A.J.*, **91**, 822.

Harris, W.E. 1987, *Pub. Astron. Soc. Pac.*, **99**, 1031.

Harris, W.E. 1988a, in *Globular Cluster Systems in Galaxies (IAU Symposium No. 126)*, eds. J.E. Grindlay and A.G.D. Philip, (Dordrecht: Reidel), p. 237.

Harris, W.E. 1988b, in *The Extra-Galactic Distance Scale*, eds. S. van den Bergh and C.J. Pritchet, (Provo: BYU Press) p. 231.

Hesser, J.E. 1988, in *Progress and Opportunities in Southern Hemisphere Optical Astronomy*, ASP Conference Series Vol. 1, eds. V.M. Blanco and M.M. Phillips..

Jacoby, G.H. 1989, *Ap.J.*, **339**, 39.

Landolt, A. 1983, *A.J.*, **88**, 439.

Madore, B.F. 1980, in *Globular Clusters*, eds. D.A. Hanes and B.F. Madore (Cambridge University, Cambridge), p. 21.

Mihalas, D., and Binney, J. 1981, in *Galactic Astronomy*, (W.H. Freeman and Company, San Francisco), p. 356.

Pierce, M.J., and Tully R.B. 1988, *Ap.J.*, **330**, 579.

Pritchet, C.J., and van den Bergh, S. 1985, *Ap.J.*, **90**, 2027.

Ratnatunga, K.U., Bahcall, J.N., and Casertano, S. 1989, *Ap.J.*, **339**, 106.

Sandage, A. 1978, *A.J.*, **83**, 904.

Stetson, P.B. 1987, *Pub. Astron. Soc. Pac.*, **99**, 191.

Stetson, P.B., and Harris, W.E. 1988, *A.J.*, **96**, 909.

Sulentic, J.W. and Tifft, W.G. 1973 in *The Revised New General Catalogue of Nonstellar Astronomical Objects* (The University of Arizona Press: Tucson Arizona), p. 240.

Strom, S.E., Forte, J.,C., Harris, W.E., Strom, K.,M., Wells, D.C., and Smith, M.,G. 1981, *Ap.J.*, **245**, 416.

Tonry, J., and Schneider, D.P. 1988, *A.J.*, **96**, 807.

Tremaine, S.D., Ostriker, J.P., and Spitzer Jr., L. 1975, *Ap.J.*, **196**, 407.

Tully, R.B., and Shaya, E.J. 1984, *Ap.J.*, **281**, 31.

Tully, R.B. 1988, in *Nearby Galaxies Catalog* (Cambridge: Cambridge University), p. 134.

van den Bergh, S., Hesser, J.E., and Harris, G.L.H. 1981, *A.J.*, **86**, 24.

van den Bergh, S. 1985, *Ap.J.*, **297**, 361.

Webbink, R. 1985, in *Dynamics of Star Clusters (IAU Symposium No. 113)*, eds. J. Goodman and P. Hut, (Dordrecht: Reidel), p. 541.

Appendix A

Image Classification

Use of the CLASSIFY subroutine written by W.E. Harris was instrumental in flagging potential non-stellar objects, thus adding a level of objectivity to the culling procedure. When plotting the roundness moment (R, see § 2.III.B) versus the magnitude, one can see a clearly defined sequence near R = 0 occupied by the stellar objects (Fig. 14), with objects scattered above this sequence. From a study of these plots it was decided that objects with R $\geq$ 1 merited further investigation. Unfortunately it was not possible to immediately eliminate all such objects because crowding effects (i.e., two or more stars in close proximity) can result in high values of R for stellar objects.

Each object with R $\geq$ 1 was scrutinized by eye on an image display, and a contour plot was constructed. Contour plots are extremely useful in finding criteria enabling one to establish whether an object is or is not stellar in appearance (see § 2.III.B). Fig. 15 shows two contour plots of objects with R $\geq$ 1. The top plot was deemed to be two stars in close proximity. Note the asymmetrical shape, and the lack of extended structure. The bottom plot was judged to be a galaxy. Note the symmetrical shape and extended structure. Fig. 16 contains a contour plot of a PSF star.

Not all culled objects are actually galaxies. There are three other categories of objects which are eliminated. The first of these are objects that, although detected by FIND, are too faint to be classified by the program, or by eye. The second arises from improper subtraction of very bright stars (i.e., stars having intensities extending into the non-linear regime of the CCD). These can produce numerous spurious faint detections in their vicinity on the second pass of DAOPHOT. The

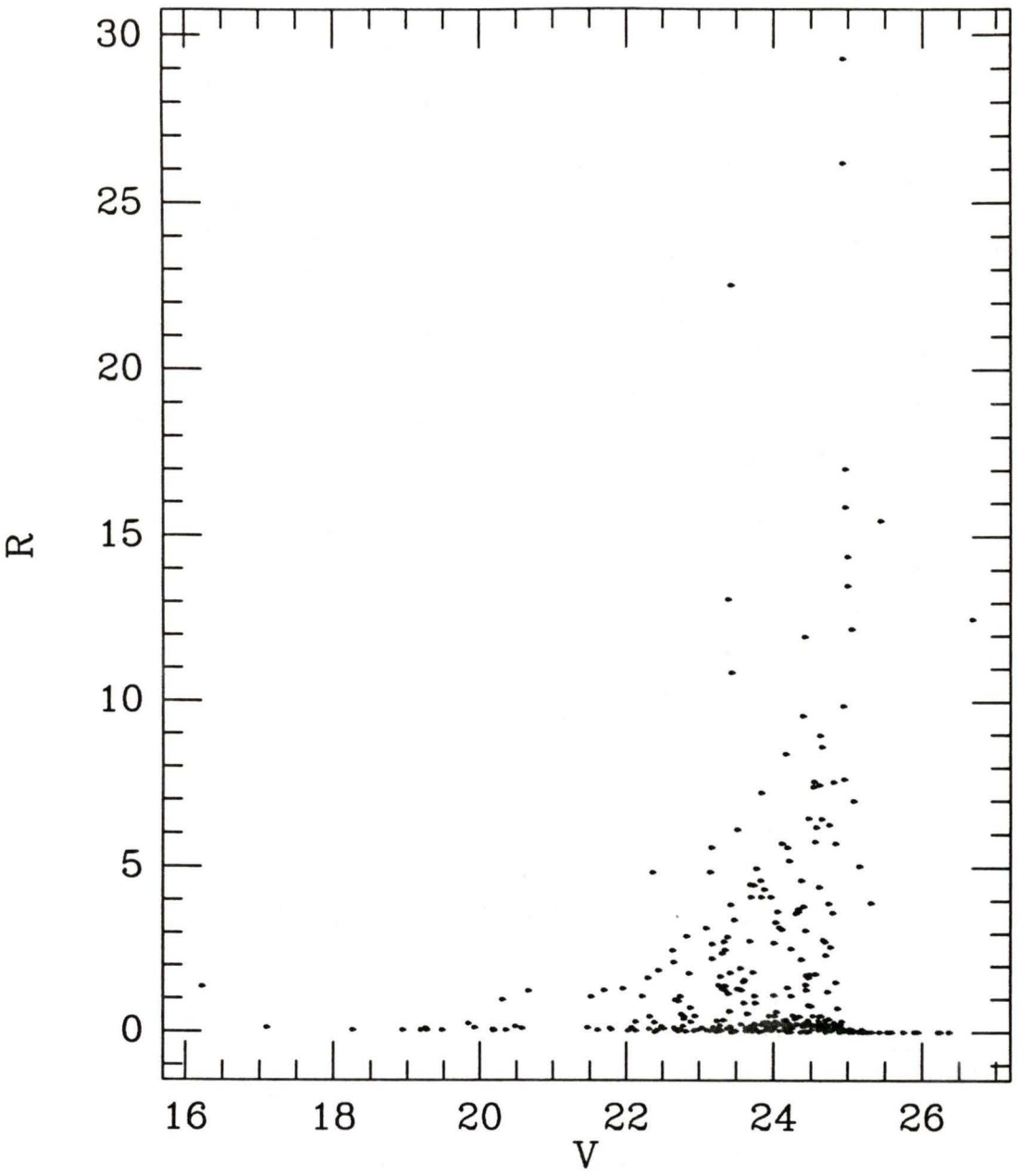

Fig. 14– Plot of the roundness parameter against V for GAL NE.

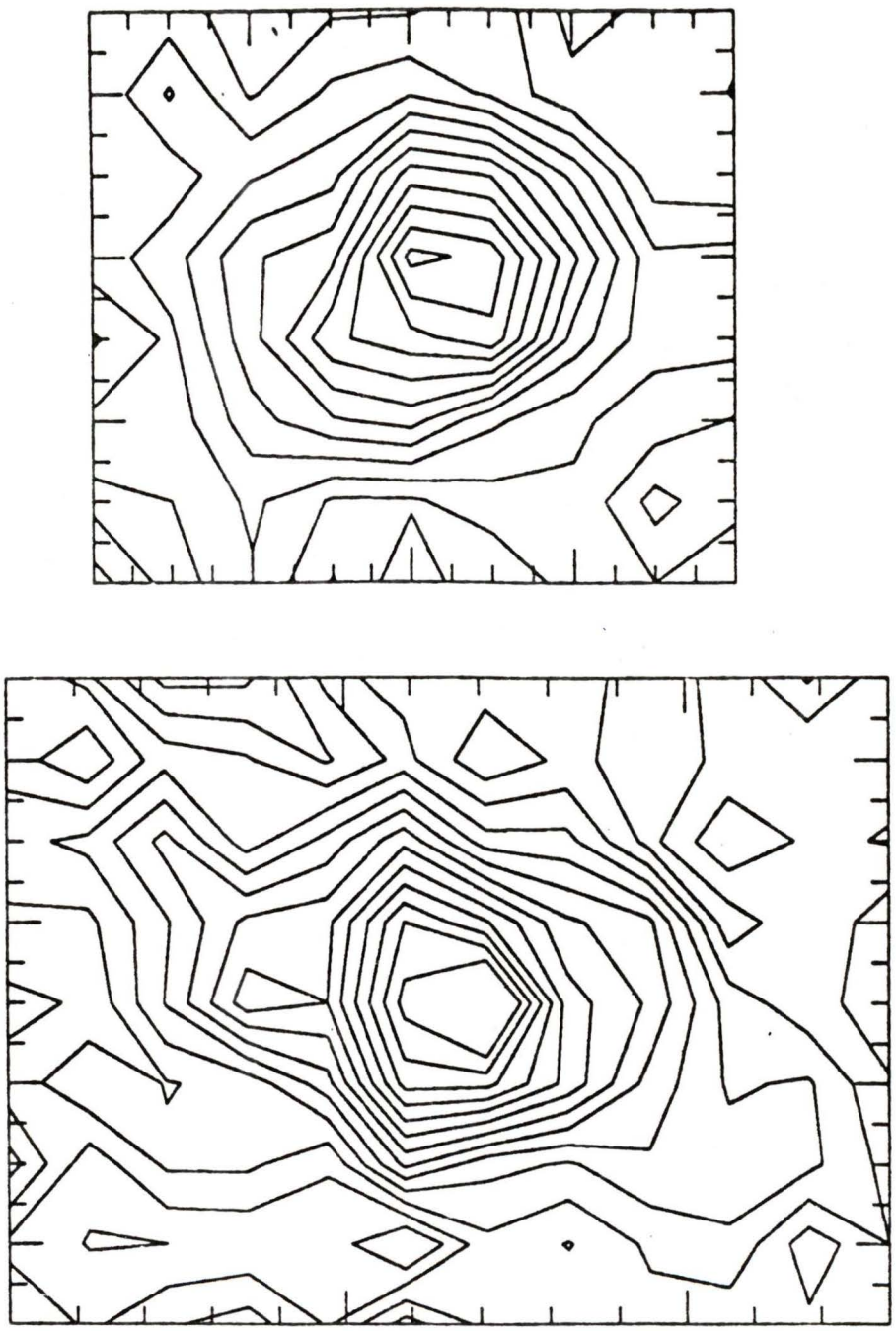

Fig. 15– Contour plots of two objects with roundness parameters exceeding 1. The top one was judged to be two stars, while the bottom one was judged to be a galaxy.

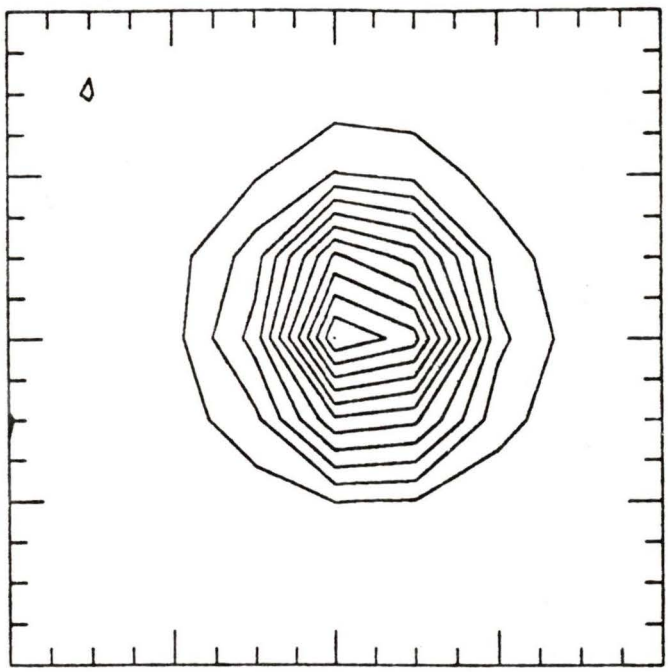

Fig. 16– Contour plot of a PSF star.

last category arises from objects which are sufficiently close to flaws on the CCD that both classification and brightness are in doubt. Table 15 shows the results of the classification; columns 2 and 3 display the number of eliminated detections for each field, and column four contains the number of remaining detections.

Table 15

Classification Results

Field	Non-Stellar	Too Faint	Remaining
GAL SW	44	27	111
GAL NW	53	44	171
GAL NE	69	32	257
BKGD SW	79	50	218
BKGD NE	64	45	163

Appendix B

Calibration

Before the transformation equations can be applied (§ III.C), corrections to the instrumental photometry zero-points must be made. These arise because the standard stars are measured using an aperture of radius 25 pixels, while only the light within two pixels of the centre is measured for the program objects. This means that some of the luminosity in the profile wings is being missed, and corrections must be made to get the program objects on to the standard system. The amount of light missed varies from frame to frame due to different seeing conditions, and therefore the aperture corrections must be obtained independently for each frame.

The first step in determining the aperture correction was the selection of roughly 20 bright uncrowded, unsaturated, stars from the program frames. All other stars were subtracted from the frame using SUBSTAR. Aperture photometry was then performed on the bright stars, with aperture sizes varying from that used on the program stars to that used on the standard stars. The difference in magnitudes was then tabulated using the program GROWTH (Stetson 1988, private communication). This program allows one to reject stars, or parts of stars, which appear contaminated with light from other sources by highlighting those stars which have light distributions deviating significantly from the mean. The correction factor was then applied to the photometry lists. The photometry should now be consistent with that obtained from the standard stars, and therefore the transformation coefficients can be applied (see § 2.III.C). Table 16 shows the size of the aperture corrections for each frame.

As there are regions of overlap on the galaxy frames, it is possible to compare

Table 16

Aperture Corrections

Field	Correction	σ
GAL SW	–0.2822	0.0115
GAL NW	–0.2253	0.0070
GAL NE	–0.1369	0.0054
BKGD SW	–0.3067	0.0106
BKGD NE	–0.2741	0.0131

the calibrated photometry for multiple detections of the same star. Tables 17, 18, and 19 are listings of stars that have been detected on two or more of the frames. There is very little systematic difference (of order 0.025 magnitudes, less than 1σ from 0 in each case), but there is a fair amount of scatter (of order 0.15) magnitudes. It should be noted that these stars are all relatively near the galaxy with its inherently high noise. For the most part, they are also near the magnitude cut-off limits of each frame, and therefore, one would expect that this scatter represents an upper limit for the photometric error.

Table 17

$V_{SW} - V_{NW}$

X	Y	V_{SW}	$V_{SW} - V_{NW}$
258.77	7.47	23.76	–0.08
293.88	58.04	17.82	0.03
280.32	90.89	20.04	0.03
284.87	139.19	23.77	–0.01
273.64	221.95	23.23	–0.05
274.45	229.86	23.74	0.35
272.08	229.92	23.18	–0.11
276.99	237.61	20.06	0.02
Mean			0.02
σ			0.14

Table 18

$V_{SW} - V_{NE}$

X	Y	V_{SW}	$V_{SW} - V_{NE}$
273.64	221.95	23.23	0.14
274.45	229.86	23.74	0.36
272.08	229.92	23.18	0.01
276.99	237.61	20.06	0.14
289.90	267.88	23.48	0.08
298.49	288.43	23.24	–0.08
278.11	292.29	23.28	0.09
263.56	292.51	23.68	–0.22
270.02	323.36	23.65	–0.19
Mean			0.04
σ			0.18

Table 19

$V_{NW} - V_{NE}$

X	Y	V_{NW}	$V_{NW} - V_{NE}$
271.94	229.91	23.29	0.12
273.77	222.06	23.28	0.18
274.36	229.71	23.39	0.01
277.11	237.59	20.03	0.11
301.22	242.08	23.95	–0.21
312.04	215.27	23.85	0.23
319.51	205.94	23.26	–0.03
329.10	250.60	23.77	–0.25
352.28	217.65	19.36	0.11
395.12	247.87	24.06	0.21
400.59	241.24	23.83	0.27
416.55	217.16	24.16	–0.20
419.09	236.99	23.74	–0.19
422.54	208.38	22.01	–0.11
432.41	224.61	23.92	–0.28
441.90	237.01	24.29	0.15
442.32	212.12	24.17	0.09
451.98	229.29	19.94	0.11
452.26	216.87	19.22	0.04
485.43	225.64	24.00	0.06
518.82	212.82	22.84	0.06
530.41	246.03	23.23	0.08
543.48	217.21	23.94	–0.08
Mean			0.02
σ			0.16

Appendix C

Artificial Star Simulations

Aside from allowing one to estimate levels of completeness for photometry, artificial star simulations enable one to check if systematic errors are being introduced. Tables 20, 21, 22, and 23 show the average and standard deviation of ΔV for each bin for the Inner and Outer regions of the three galaxy frames, and for the entire area of the two background frames. The last row in each table shows the slope ($\frac{\Delta V}{V}$) and its error for least-squares fits to the data, for those bins used in the luminosity function (§ 2.III.D). In all cases the slope has a negligible value, although generally it is positive (there are two exceptions to this: GAL NW Outer, and GAL NE Inner). In each case, the tables list values for the bin one fainter than the cut-off adopted in the analysis (between the horizontal lines in the tables), and it can be seen that in general both ΔV and scatter increase greatly for this bin, supporting the choice of cut-off bin.

Table 20

Photometry Residuals for GAL SW

		Inner			Outer	
Bin	N_{rec}	$\langle \Delta V \rangle$ ($\times 10^{-4}$)	σ ($\times 10^{-4}$)	N_{rec}	$\langle \Delta V \rangle$ ($\times 10^{-4}$)	σ ($\times 10^{-4}$)
17.75	7	−1.4	3.5	19	−1.1	3.1
18.25	18	2.2	6.3	23	−2.6	9.0
18.75	14	−1.4	19.2	32	−3.4	16.3
19.25	21	−4.3	13.3	42	2.1	7.7
19.75	18	4.4	18.3	47	2.1	39.8
20.25	19	−2.1	8.9	61	5.4	44.8
20.75	25	−16.4	66.3	76	−7.9	52.3
21.25	35	43.7	163.1	105	9.0	114.5
21.75	39	7.7	156.2	79	10.3	126.6
22.25	46	23.0	221.9	114	−20.0	178.6
22.75	41	42.4	164.2	92	−32.5	180.8
23.25	52	75.4	326.4	112	19.6	362.0
23.75	45	109.3	441.3	80	49.9	360.8
24.25	15	590.0	1209.9	39	1773.3	9088.2
Slope		0.5	0.2		0.7	0.1

Table 21

Photometry Residuals for GAL NW

		Inner			Outer	
Bin	N_{rec}	$\langle \Delta V \rangle$ ($\times 10^{-4}$)	σ ($\times 10^{-4}$)	N_{rec}	$\langle \Delta V \rangle$ ($\times 10^{-4}$)	σ ($\times 10^{-4}$)
17.75	3	3.3	4.7	16	–423.1	1580.3
18.25	5	0.0	0.0	36	6.9	30.9
18.75	8	–1.3	3.3	34	3.8	14.1
19.25	8	–2.5	6.6	56	–2.9	15.6
19.75	13	–7.7	29.7	46	–0.9	25.9
20.25	12	5.8	76.5	64	–3.4	18.2
20.75	15	54.0	79.6	67	0.3	54.9
21.25	20	27.0	64.4	103	7.7	75.8
21.75	23	25.2	163.3	93	–1.1	117.1
22.25	20	108.5	305.5	113	0.8	115.3
22.75	38	–53.4	196.7	118	–45.3	203.4
23.25	29	36.6	238.7	129	–8.4	386.5
23.75	37	158.6	365.5	126	11.5	444.3
24.25	13	268.5	655.5	117	200.5	726.9
24.75	4	2415.0	2510.5	35	2441.7	10439.4
Slope		1.5	0.4		–0.1	0.2

Table 22

Photometry Residuals for GAL NE

		Inner			Outer	
Bin	N_{rec}	$\langle \Delta V \rangle$ ($\times 10^{-4}$)	σ ($\times 10^{-4}$)	N_{rec}	$\langle \Delta V \rangle$ ($\times 10^{-4}$)	σ ($\times 10^{-4}$)
19.25	14	–102.1	121.6	33	–61.8	107.5
19.75	34	–69.4	121.2	38	–65.0	117.8
20.25	39	-45.1	144.1	50	–58.8	120.8
20.75	42	–49.8	114.2	55	–92.5	150.1
21.25	46	–49.3	204.0	52	–32.9	105.3
21.75	57	–52.8	135.2	62	–55.3	129.2
22.25	48	–30.6	91.5	63	–24.6	267.7
22.75	72	6.7	322.1	78	-67.8	198.1
23.25	68	–35.3	291.0	92	–13.5	260.8
23.75	69	25.2	587.1	91	31.1	586.8
24.25	67	–25.2	827.9	11	–7.9	626.0
24.75	44	183.2	568.2	66	207.7	736.1
25.25	23	4328.6	12820.4	12	147.5	588.9
Slope		–9.2	0.3		11.0	0.6

Table 23

Photometry Residuals for BKGD SW and BKGD NE

	BKGD SW			BKGD NE		
Bin	N_{rec}	$\langle \Delta V \rangle$ ($\times 10^{-4}$)	σ ($\times 10^{-4}$)	N_{rec}	$\langle \Delta V \rangle$ ($\times 10^{-4}$)	σ ($\times 10^{-4}$)
18.25	15	–0.7	14.4	8	1.3	9.3
18.75	27	–4.8	10.3	16	0.0	11.2
19.25	38	0.8	13.8	31	2.9	15.1
19.75	39	–1.0	24.5	42	–4.8	22.0
20.25	42	–4.5	27.9	40	–2.3	24.1
20.75	50	34.8	313.7	51	0.2	32.2
21.25	52	–4.2	53.2	38	8.7	52.2
21.75	77	–9.4	108.1	55	3.8	81.9
22.25	81	24.9	189.0	65	–10.8	87.5
22.75	62	13.2	128.3	74	53.0	175.1
23.25	94	28.8	209.5	71	–15.4	228.5
23.75	99	–44.5	341.6	90	8.8	184.4
24.25	10	189.8	646.5	77	71.9	545.9
24.75	71	287.0	1025.8	84	78.9	604.9
25.25	17	899.4	2716.5	30	1117.3	1663.9
Slope		2.6	2.1		1.4	2.2

Appendix D

Distance Determination

In order to derive parameters for the Milky Way GCLF that would be consistent with the luminosity function of NGC 5170, it was felt that the Milky Way data should be treated in a similar fashion. To this end, the Milky Way data, taken from Webbink (1986), were binned using the same 0.5 mag bin width as used for NGC 5170. This is important since binning data can introduce biases into the fit, and thus, more consistent parameters will be derived if the biases are mimicked in the Milky Way sample. The three-parameter least-squares fit (see § VI.A) yielded A = 22.06 ± 0.57, M_{V_o} = –7.20 ± 0.04, σ = 1.28 ± 0.05 and is illustrated in Fig. 17.

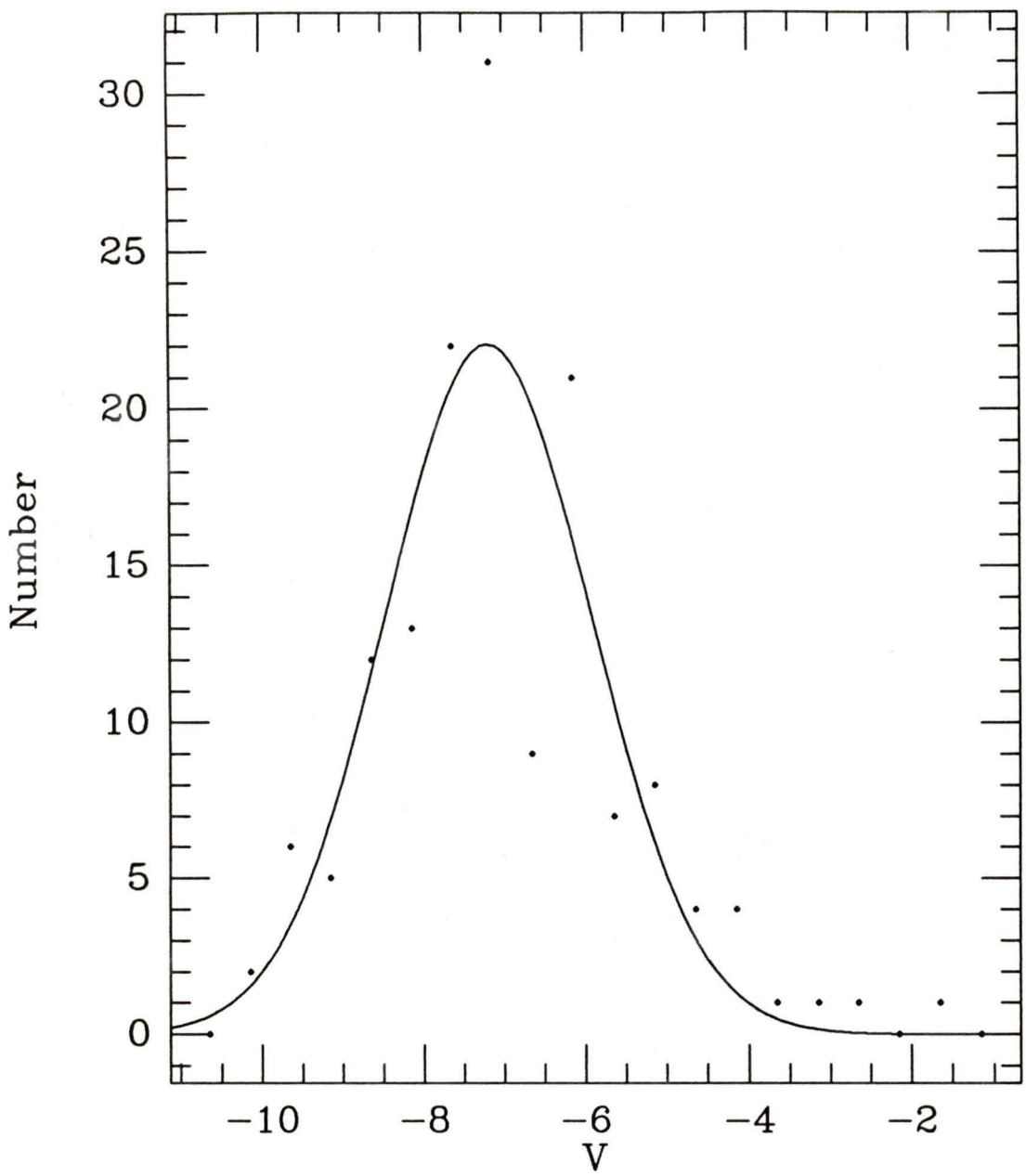

Fig. 17– The Milky Way globular cluster luminosity function. The solid line is the best-fit gaussian with parameters A = 22.06 ± 0.57, $M_{V_\circ}$ = –7.20 ± 0.04, σ = 1.28 ± 0.05.

Glossary

Charge Coupled Device (CCD). An electronic detector used for counting photons. In astronomy it is used to produce an electronic "photograph" of a region of the sky.

Completeness Limits. Result because stars (particularily faint ones) are missed in the reduction procedure. Necessitates the use of "completeness corrections".

Defringing. The removal of interference patterns from a CCD image by subtracting out a standard fringe frame.

Diameter-velocity-dispersion Relation. Used to determine the intrinsic diameter of elliptical galaxies from measurements of their velocity dispersions. Commonly used in conjunction with the apparent angular diameter of the galaxies to derive their distances.

Dynamical Friction. A process whereby globular clusters passing close to the galaxy centre lose angular momentum and eventually spiral inwards.

Extinction. The phenomenon whereby photons of light are absorbed by the interstellar medium. This causes the brightness of objects to be underestimated, necessitating the use of "extinction corrections".

Fisher-Tully Relation. A method of determining the intrinsic brightness of disk galaxies from radio wavelength measurements of their rotation curve. Commonly used in conjunction with the galaxies' apparent brightness to derive distances.

Flat-fielding. The process of removing low frequency and pixel-pixel variations intrinsic in a CCD by dividing out a uniformly illuminated CCD image.

Luminosity Fluctuation Method. Use of an analysis of the noise of a

CCD frame containing a galaxy to determine its distance.

Luminosity Function (LF). A plot of number of objects against luminosity. Usually, the luminosity is expressed in terms of the standard astronomical magnitudes (a logarithmic scale).

Median Filter. A data-smoothing process where a pixel on a CCD is assigned a value equal to the median of the intensities of nearby pixels.

Photometry. The process of measuring the brightness of astronomical objects. The light is usually measured in a specific spectral region, and converted to a standard system using stars of known luminosities.

Planetary Nebula Method. Involves construction of the planetary nebula luminosity function for a galaxy to derive its distance.

Radial Velocity. The velocity of an object either towards or away from the earth.

Seeing. The angular full-width-half-maximum of a stellar (unresolved) profile. It is determined by atmospheric conditions and instrumental effects. Generally, "seeing" of less than 1 arcsecond is considered excellent.

Spiral Galaxy. A galaxy that exhibits a disk like structure with bright "arms" emanating from the nuclear region. Generally considered to consist of three separate components: a flat disk, a central bulge, and an extended spherical halo.

Vita

Surname: **Fischer** Given Names: **Philippe**

Place of Birth: **Montreal, Quebec** Date of Birth: **Feb. 17, 1964**

Educational Institutions Attended, with Dates of Entering and Leaving:

McMaster University, Hamilton **1983** to **1987**

University of Victoria, Victoria **1987** to **1989**

Degrees, Diplomas, Etc., Awarded, with Dates and Names of Institutions:

B.Sc. (Honours) **1987** **McMaster University**

Honours and Awards:

H.L. Hooker Scholarship 1984/85

NSERC Undergraduate Research Award 1985

Yates Scholarship 1985/86

Boyd McLay Scholarship 1986/87

University Scholarship 1986/87

NSERC Postgraduate Scholarship 1987/88

U. of Victoria President's Award 1987/88

NSERC Postgraduate Scholarship 1988/89

U. of Victoria President's Award 1988/89

Publications:

—**Antibonding σ^* Valence MOs in the Inner-Shell and Outer-Shell Spectra of the Fluorobenzenes**: Hitchcock, A.P., Fischer P., Gedanken, A., and Robin, M.B. 1987, *Journal of Physical Chemistry* **91**, 531.

—**Resonances in the K-Shell Spectra of Fluorinated Organic Molecules**: Hitchcock, A.P., Fischer, P., and McLaren, R. 1987, in *Giant Resonances in Atoms, Molecules and Solids*, p. 281.

—**Electronic Excitation and π-Electron Interaction in Borazine**: Doering, J.P., Gedanken, A., Hitchcock, A.P., Fischer, P., Moore, J., Olthoff, J.K., Tossell, J., Raghavachari, K. and Robin, M.B. 1986, *Journal of the American Chemical Society* **108**, 3602.

Partial Copyright License

I hereby grant the right to lend my thesis (the title of which is shown below) to users of the University of Victoria Library, and to make single copies only for such users, or in response to a request from the library of any other university or similar institution, on its behalf or for one of its users. I further agree that permission for extensive copying of this thesis for scholarly purposes may be granted by me or a member of the university designated by me. It is understood that copying or publication of this thesis for financial gain shall not be allowed without my written permission.

Title of Thesis:

The Globular Cluster System of the Edge-On Spiral Galaxy NGC 5170

Author

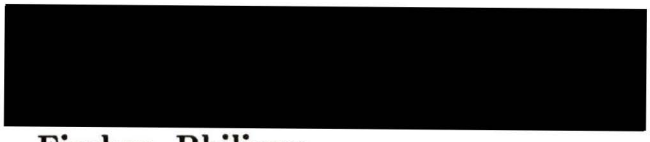

Fischer, Philippe

June 1, 1989

ISBN 0-315-53712-4